RESERVOIR PREDICTION FROM MULTICOMPONENT SEISMIC DATA, RULISON FIELD, PICEANCE BASIN, COLORADO

By

Elizabeth Ann LaBarre

A thesis submitted to the Faculty and Board of Trustees of the Colorado School of Mines in partial fulfillment of the requirements for the degree of Master of Science (Geophysical Engineering).

Golden, Colorado
Date August 29, 2008

Signed: _____
Elizabeth A. LaBarre

Signed: _____
Dr. Thomas L. Davis
Thesis Advisor

Golden, Colorado
Date August 29, 2008

Signed: _____
Dr. Terence K. Young
Professor and Head
Department of Geophysics

ABSTRACT

Shear-wave (S-wave) seismic acquired at Rulison Field, Piceance Basin, Colorado by the Reservoir Characterization Project in 2003 exhibits evidence of anisotropy due to faults and natural fractures from reflection discontinuity and S-wave splitting analysis. Rulison Field is an unconventional natural gas reservoir producing from the fluvial tight gas sandstones of the Late Cretaceous Williams Fork Formation.

Fault interpretations were made from multicomponent seismic data. The compressional and shear wave data clearly show faults in the Cameo Coal interval in dominate a north-northwest direction. The shear-wave seismic shows evidence of these faults propagating upward into the main reservoir interval. Borehole image logs confirm the existence of these faults. Wrench faults splay upward into the reservoir as flower structures that control fracturing within the reservoir.

Innovative S-wave splitting techniques were used to calculate seismic anisotropy within the reservoir interval. High S-wave seismic anisotropy is caused by high natural fracture density. Borehole anisotropy measurements calculated from cross-dipole sonic logs and fracture intensity from borehole image logs confirm that the surface S-wave seismic is capable of delineating zones of high natural fracture density in the reservoir interval. Anisotropy volumes provide previously unknown information about natural fracturing that can ultimately be used to optimize well locations and increase natural gas recovery.

TABLE OF CONTENTS

LIST OF FIGURES

LIST OF TABLES

ACKNOWLEDGEMENTS

The Reservoir Characterization Project (RCP) at Colorado School of Mines (CSM) sponsored this research. I would like to acknowledge and thank the RCP for the data, support, and guidance that made this thesis possible. I would also like to thank the RCP sponsors for there financial support and recommendations, specifically Williams Production Company and Transform Software™.

I would also like to thank my thesis committee Dr. Tom Davis, Dr. Bob Benson, Dr. Mike Batzle, and Dr. Steve Hill. Their input and advice guided the path of my research and expanded my understanding of geophysics. I would also like to single out Dr. Tom Davis to specifically thank him for believing in my abilities to complete this thesis even when I doubted them. His drive to pursue challenging problems and state of the art technologies motivated me to explore the vast possibilities of geophysics and gave me a solid foundation in geophysics.

I would additionally like to acknowledge all of the professors, students, and staff in the Geophysics department at CSM for their support specifically the RCP graduate students that helped and contributed to this research.

And, finally, last but certainly not least, I would like to thank my family and friends for their encouragement and support. Specifically, I would like to thank Chris Emanuel and Caroline LaBarre who were always available to help me through the rough times and motivate me to finish.

CHAPTER 1 INTRODUCTION

Rulison Field, Piceance Basin, Colorado was chosen by the Reservoir Characterization Project (RCP) to investigate the ability of multicomponent seismic to detect the presence of faulting and natural fractures in tight gas sand reservoirs. Traditionally, multicomponent seismic has not been used in unconventional reservoirs. This thesis, as one element of the RCP study, presents research and results of imaging reservoir level faulting from shear-wave (S-wave) seismic and detecting natural fracturing from S-wave splitting analysis.

The goal of the RCP study at Rulison Field is to optimize natural gas recovery using multicomponent and time-lapse seismic to characterize and model the reservoir. To accomplish this goal, the RCP acquired three 9-component seismic surveys at Rulison Field. The focus of this thesis is the identification of faulting and areas of natural fracturing in the thick reservoir interval of Rulison Field from the first multicomponent seismic survey.

Rulison Field is a thick tight gas sand reservoir that is heavily faulted and fractured. The reservoir rock consists of stacked fluvial sandstones and shales approximately 2000 feet thick. The sandstones are discontinuous and typically below seismic resolution. The reservoir level faults and fractures have proven to be difficult, if not impossible, to map with conventional P-wave seismic. Typical P-wave horizon based structural interpretation through the reservoir is not viable due to the heterogeneous nature of the rock and with little to no vertical offset of the faults. Therefore, a more

robust way of imaging the reservoir structure and fractures is necessary. This is the motivation behind this research. This research tests the limits of S-wave seismic imaging and shows that S-wave seismic data provides extensive information about the structural properties of Rulison Field, primarily faulting and natural fractures.

1.1 Geologic Background

Rulison Field is located in the Piceance Basin of western Colorado along the Colorado River near the town of Rifle (figure 1.1). The Piceance Basin has an estimated 311 trillion cubic feet (TCF) of original gas in-place (OGIP) (Kuuskraa et al., 1997). 106 TCF of this OGIP exists in four fields in the east-central portion of the basin, Rulison, Mamm Creek, Parachute and Grand Valley. Sixty to eighty percent of this gas is estimated to be recoverable (Toal, 2005). These fields, shown in figure 1.1, are unconventional tight gas sand fields within the basin-centered gas accumulation. They produce from lenticular, fluvial sandstones and coals of the Late Cretaceous Williams Fork Formation. The reservoir sandstones are referred to as ‘tight’ because they have extremely low matrix permeability, typically in the microdarcy range. Natural fractures are apparent in certain locations in core and image logs. These natural fractures increase the permeability of the reservoir system by one to two orders of magnitude (Lorenz, 2003). Without these natural fracture networks, and modern hydraulic fracturing, these reservoirs would not produce economic quantities of natural gas due to the lack of matrix permeability. The performance of better wells generally correlates to the existence of open natural fracture networks connected to the wellbore.

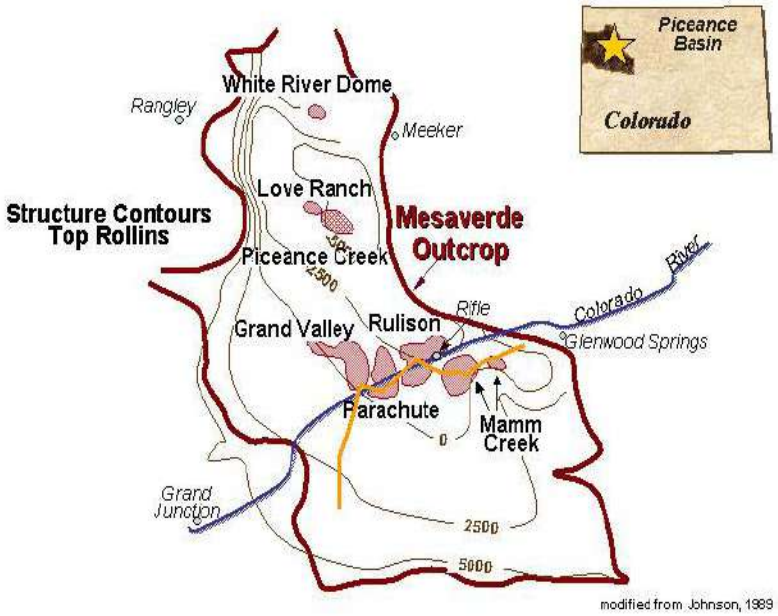

Figure 1.1. Map of the Piceance Basin showing the major gas fields. The edges of the basin where the Mesaverde Formation outcrops are drawn in red, and the top of the Rollins sandstone is contoured. (Williams Production Co.)

1.1.1 Stratigraphy

The reservoir rock in Rulison Field is the Williams Fork Formation of the Cretaceous age Mesaverde Group. Figure 1.2 shows a stratigraphic column of the Mesaverde Group. Deposition of the Mesaverde Group occurred during the Late Cretaceous in the Rocky Mountain Foreland Basin. This immense basin covered much of the western interior of North America including the entire Piceance Basin and surrounding mountain basins until the Laramide Orogeny subdivided it into the many smaller mountain basins that exist today. The Sevier Mountains bounded the Rocky Mountain Foreland Basin on the west and the Cretaceous Seaway bounded the basin to the east. Figure 1.3 shows a paleogeographic reconstruction of the depositional environment of the Mesaverde Group in the Rocky Mountain Foreland Basin.

The Iles Formation is the oldest formation of the Mesaverde Group. This formation is not currently a major drilling target in Rulison Field, but may be in the future since the formation is known to be a productive, gas bearing formation in neighboring Mamm Creek. The deposition of the Iles Formation occurred on the western edge of the Cretaceous Seaway during regressive cycles of the Cretaceous Seaway. The Iles Formation includes three regressive marine sandstones members, the Corcoran, the Cozzette, and the Rollins. These sandstones are laterally continuous and correlate throughout most of the Piceance Basin. All three of these sandstones are interbedded between Mancos Shale deposited as the seaway transgressed over the area after the regressions that allowed for the deposition of these marine sandstones.

The Williams Fork Formation is the youngest formation in the Mesaverde Group and is the producing reservoir rock in Rulison Field. This formation was deposited primarily in a coastal plain environment once the Cretaceous Seaway completely regressed. The Cameo Coal interval is the lowest unit in the Williams Fork and is the main source of natural gas in the Rulison Field area. The Cameo Coal unit contains widespread coals interbedded between 30- to 100-ft thick fluvial sandstones. The depositional environment alternates between coastal plain and meandering stream environment. The coastal plain environment has a high water table that allows deposition and preservation of peat (Johnson and Flores, 2003). The Cameo Coals outcrop in Coal Canyon on the western edge of the basin and are buried as deep as 9,000ft in the central part of the basin.

The portion of the Williams Fork above the Cameo Coals is the main reservoir rock for Rulison Field and the other nearby gas fields. This interval ranges from 2,800 to

3,800ft thick and was deposited in a coastal plain to alluvial plain environment with variable accommodation space. The lower part of this interval and some of the sandstones in the Cameo Coals were deposited during times of high accommodation space. This interval contains meandering stream deposits of sands, silts, and shales that are difficult, if not impossible, to correlate between closely spaced wells. These deposits are common in areas where accommodation space is high and the shoreline is transgressing. In the upper part of Williams Fork, sand and shale deposits slowly become more laterally continuous are likely from a braided stream type of environment. This suggests that accommodation rates were dropping and the shorelines were prograding with less stratigraphic rise (Cumella and Ostby, 2003).

A laterally continuous shale marker exists through most of the basin about 500 to 800ft below the top of the Williams Fork Formation. Typically, this shale has a gamma ray value that is 10-20 API units higher than the other surrounding shales and corresponds to a regionally continuous seismic reflector seen in all seismic surveys near the basin-centered gas fields. This marker is mapped through the seismic surveys as the upper Mesaverde (UMV) shale marker horizon. In the Rulison Field area, a thin coal known as the Price Coal sits about 50 ft above the shale. These two geologic markers mark the transition from isolated meandering channel type deposits to laterally more continuous deposits. The top of continuous gas saturation is always a few hundred feet below the shale marker, but often the shale marker is referenced as a possible seal for the reservoir since there is no other apparent seal that is trapping the gas in place. The reservoir for Rulison Field is typically defined as the gas saturated interval from the base

of the Cameo Coals to the top of the gas saturated zone a few hundred feet below the shale marker.

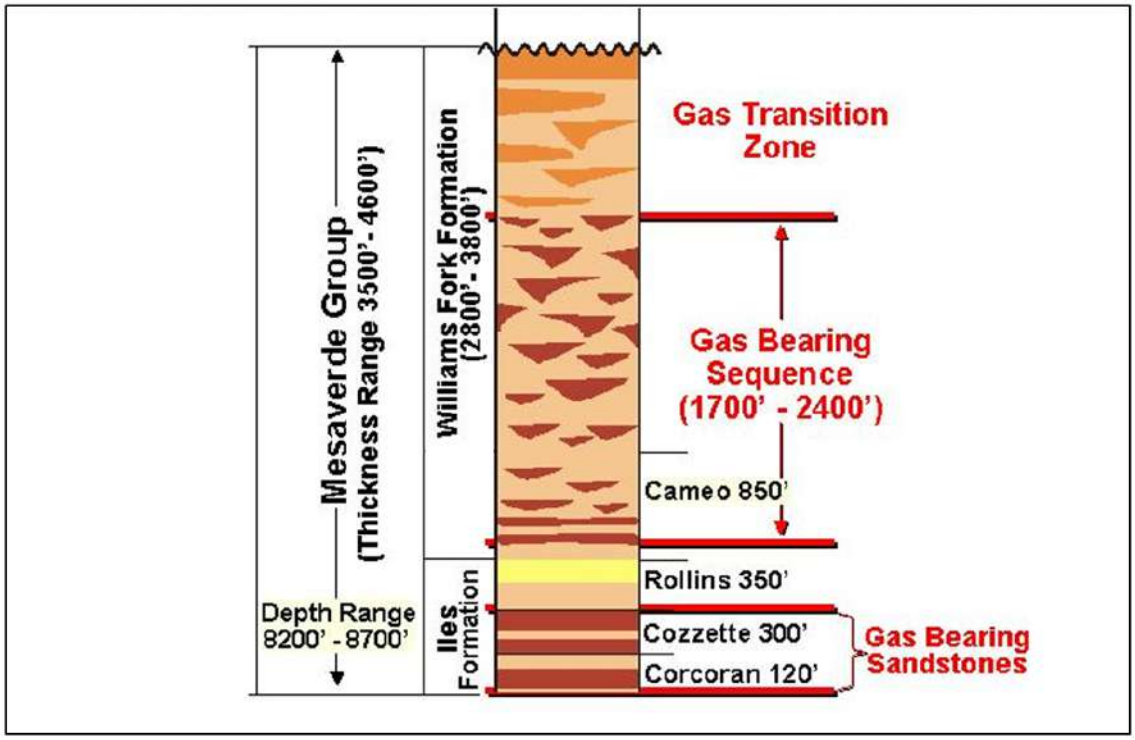

Figure 1.2. Stratigraphic column of the Mesaverde Group. Rulison Field produces from the Lower Williams Fork Formation labeled 'Gas Bearing Sequence'. (Williams Production Co.)

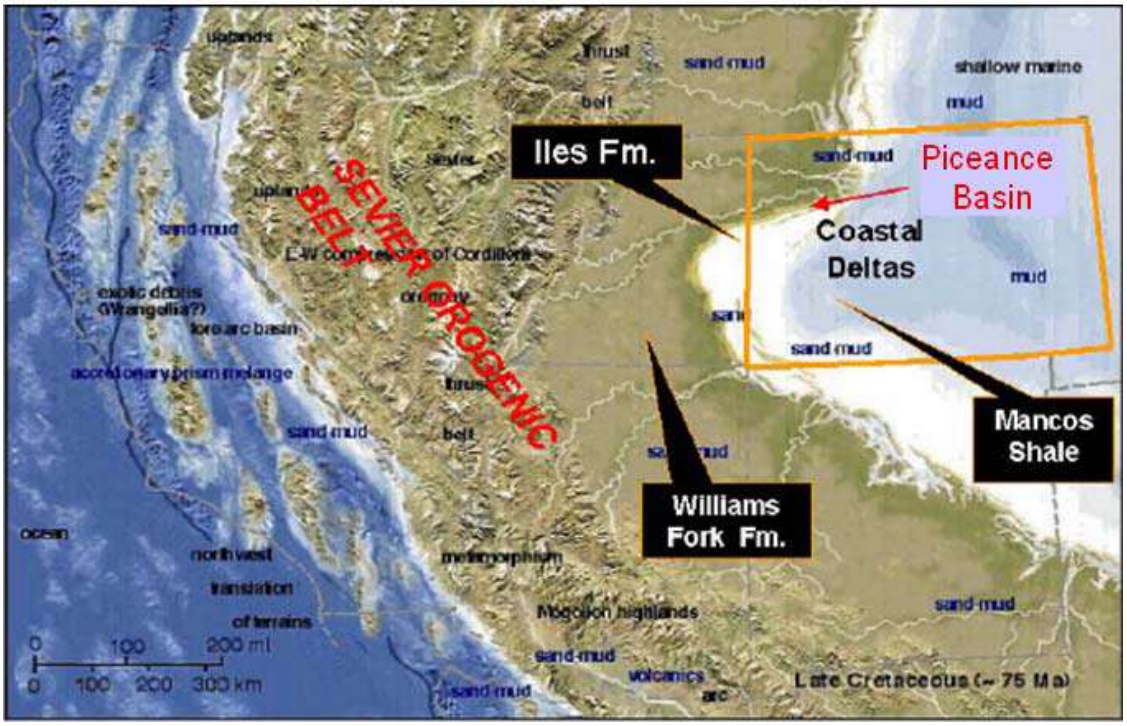

Figure 1.3. Late Cretaceous (~75Ma) paleogeographic reconstruction of western North America showing the depositional environments for the Mancos Shale, the Iles Formation, and the Williams Fork Formation. (Cumella and Ostby, 2003).

1.1.2 Structural History

The Laramide Orogeny created the Piceance Basin by isolating it from the Rocky Mountain Foreland Basin. The first evidence of the Laramide Orogeny in the Piceance Basin can be seen during the deposition of the upper Williams Fork, but the majority of the basin formation occurred later. Figure 1.4 shows a paleogeographic reconstruction of the Piceance Basin during the deposition of the Mesaverde. This figure shows that during the majority of the deposition of the Mesaverde Group there was no surface expression of the orogeny.

At the end of the Cretaceous, the Laramide Orogeny drastically changed the landscape. The Cretaceous-Tertiary unconformity is evident between the youngest members of the Mesaverde Group and the overlying Tertiary conglomerates throughout the basin. The depositional hiatus varies in length through the basin. The youngest

member of the Mesaverde Group increases in age to the west. This could be due to erosion caused by the rise of a broad arch in the western part of the basin near the modern day Douglas Creek Arch and Uncompahgre Uplift. During this time there is also evidence that the Park and Swatch ranges were beginning to rise and continued to rise until the middle Paleocene. These mountains and the broad arch are the first evidence of Laramide structure and east-west compression in the area.

At the end of the Paleocene, Laramide deformation began to affect the area again. The White River and the Uncompahgre Uplifts began to rise due to more east-west compression. By the Early Eocene, the Piceance Basin had formed between Laramide structures and very few structural changes have occurred in the basin since. The modern Piceance Basin is an asymmetrical basin that dips to the east and southeast. Figure 1.5 shows the present boundaries of the Piceance Basin. The Uncompahgre Uplift bounds the basin to the southwest, the Douglas Creek Arch to the west, the Grand Hogback to the east, the Sawatch Range and the Gunnison Uplift to the south, and the White River Dome and the Axial Basin Arch to the north.

The structural and stratigraphic histories of the Piceance Basin are very important to Rulison Field because they created the unconventional aspect of this field. Instead the natural gas is widespread through a large area of the basin. Cumella and Ostby's (2003) Piceance Basin-Centered Gas Model is shown in figure 1.6. This model shows a present-day cross-section approximately west-east from the Uncompahgre Uplift through the basin to the White River Uplift. The main gas fields of the basin, including Rulison Field, are located in the center of the basin. These fields are considered unconventional because, as the cross-section shows, an impermeable seal or conventional trap does not confine

field. This means there is no structural or stratigraphic feature that is trapping the gas in place and keeping it from migrating up dip. This type of model for a gas field goes against the conventional oil and gas field model that requires a distinct trapping mechanism to keep the hydrocarbons in the reservoir rock and from migrating up section due to fluid density contrasts. These fields have only a subtle trapping mechanism created by the extremely low permeability and capillary pressures of the reservoir rock which keeps the gas from rapidly migrating to the surface. In geologic time this is actually just a leaky seal. Natural gas in these fields is generated by the deeply buried Cameo Coals and the reservoir rock is the coals and the overlying Williams Fork sandstones. Gas saturation is highest in the Cameo Coals and slowly decreases up section through the Williams Fork.

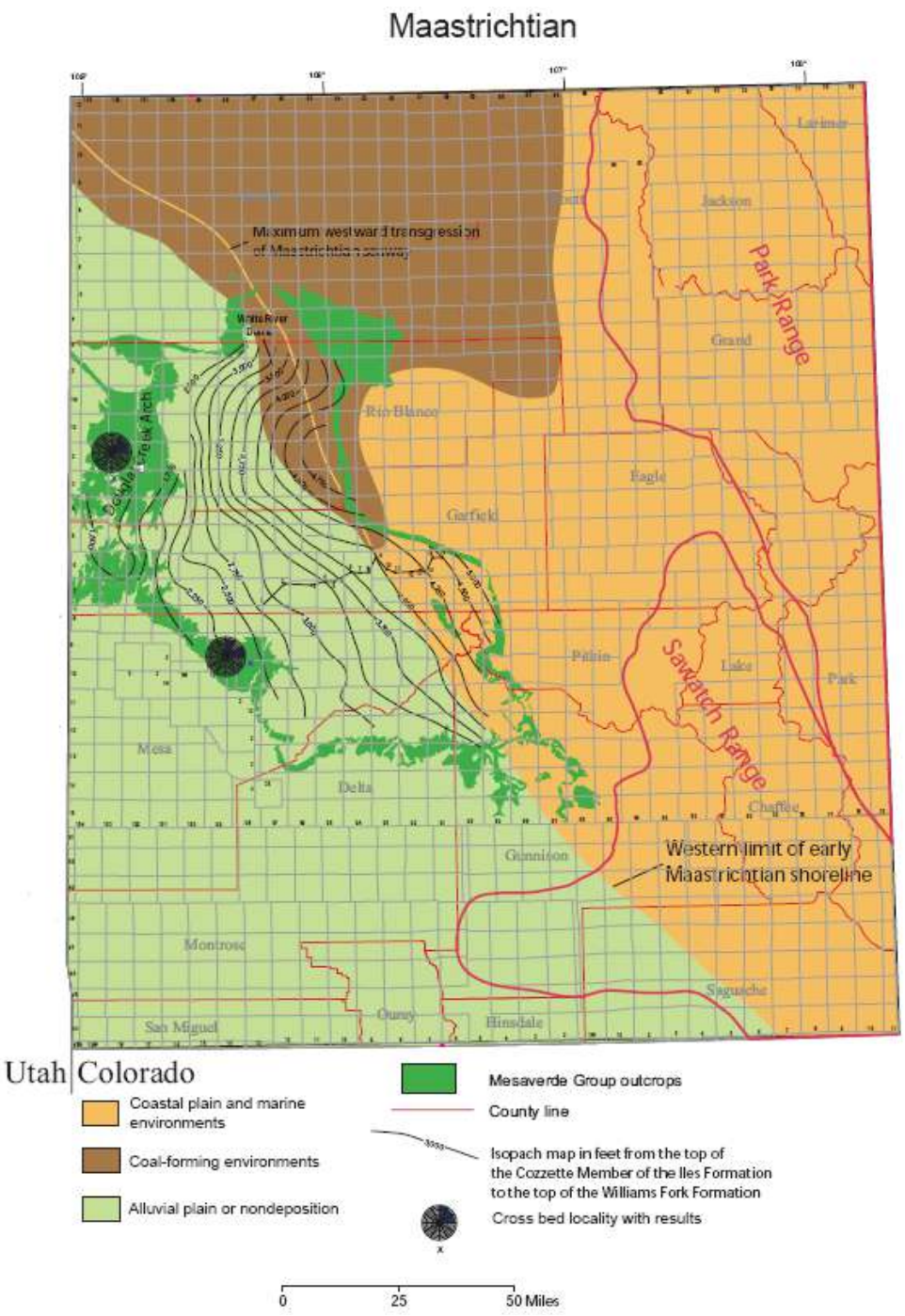

Figure 1.4. Paleogeographic reconstruction of northwest Colorado at the end of the deposition of the Mesaverde Group in the Late Cretaceous Maastrichtian age. The boundaries shown in green are the locations of where the Mesaverde Group currently outcrop and are the limits Piceance Basin. (Johnson and Flores, 2003)

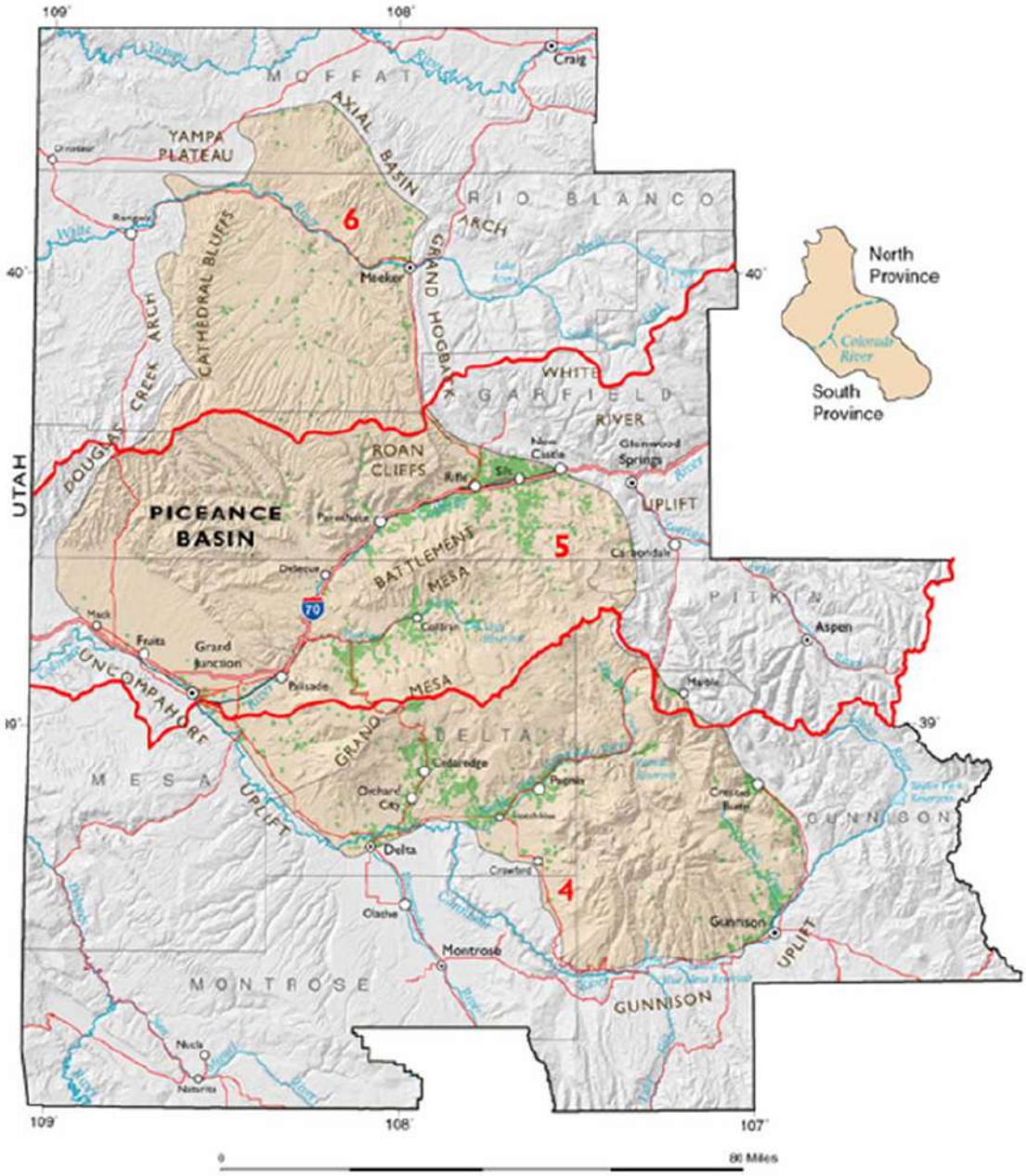

Figure 1.5 Map showing location of the Piceance Basin in northwestern Colorado and surrounding uplifts. (Topper et al., 2003)

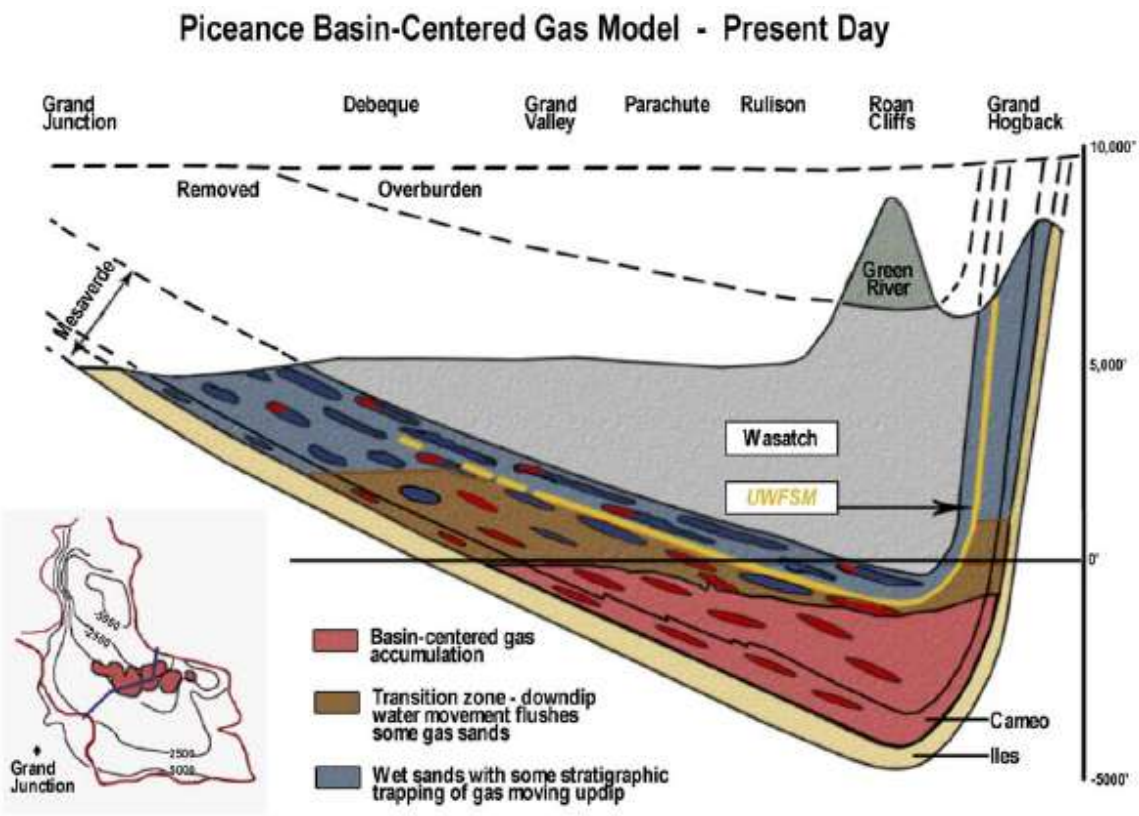

Figure 1.6 Piceance Basin-centered Gas Model (Cumella and Ostby, 2003)

1.1.3 Faulting & Natural Fracturing

Faulting and natural fracturing increase the permeability of the tight gas sandstones by creating conduits for the gas to flow from the low matrix permeability reservoir rock to the wellbore. The data that Lorenz and Finley (1991) collected confirms production increases of over two orders of magnitude occur where natural fractures are present. Therefore, locating areas with dense natural fracturing is necessary to drill the most economically successful wells. Natural fractures occur most often near deep faults and the reservoir level fault zones they create. If the reservoir level faults can be mapped, the most likely location of increased natural fracturing can be extrapolated.

Faulting in the reservoir interval of Rulison Field is very difficult to interpret from traditional P-wave seismic. Below the reservoir, deep faults can be seen in a regional P-wave seismic survey acquired by Seitel in 2001. Cumella and Ostby (2003) interpret these faults to be left-lateral wrench faults striking to the northwest and reverse faults striking to the north-northwest that were created by the east-west compression of the Laramide Orogeny. Many faults can be interpreted at the Rollins level on p-wave seismic but are extremely difficult to interpret with any confidence above this level and in the reservoir likely because of the heterogeneity of the rocks and the presence of natural gas. Jeff Jackson (2007) addresses regional faulting and basin history in more detail in his thesis.

Natural fracturing occurs in some areas of the Williams Fork Formation and is typically denser near faults and at structural flexure points occurring at changes in structural dip. Natural fractures are steeply dipping as seen in core and borehole image logs. Many of these strike parallel to the direction of maximum horizontal stress, approximately east-west, but there are other directions as well. Drilling induced fractures also trend in the east-west direction which shows that the basin is currently still under east-west compression (figure 1.7). This makes the origination of the natural fractures difficult to date since the basin has been under east-west compression since the Laramide Orogeny. Since the strike of most of the natural fractures seen in wellbores are directionally dependent they will potentially cause seismic azimuthal anisotropy. Seismic azimuthal anisotropy is best detected with S-wave seismic data.

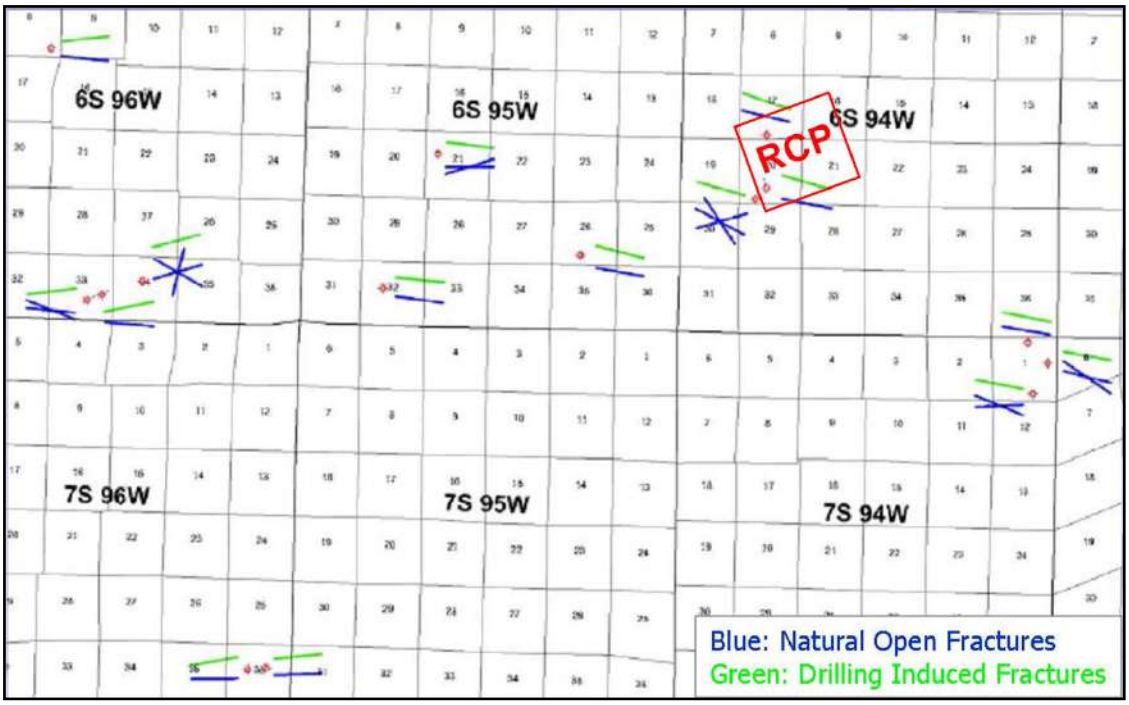

Figure 1.7. Map of the Rulison Field area showing the average strike of natural fractures from borehole image logs in blue and drilling induced fractures in green. The RCP research area is shown in red. (Modified from Cumella and Ostby, 2003)

1.2 Data

The seismic data used for this research is nine-component seismic acquired by the RCP in the fall of 2003. The RCP also acquired two other dedicated time-lapse nine-component seismic surveys in the fall of 2004 and the fall 2006. This research uses only the baseline 2003 seismic data. The RCP has also acquired other geophysical data in the seismic survey area of the field such as vertical seismic profiles, borehole micro-seismic, image logs, and cross-dipole sonic logs. Other data not collected by the RCP such as traditional well logs from wells in the field, older P-wave seismic surveys, and log and core data from the Department of Energy's Multi-well Experiment (MWX) is also being used to aid in reservoir characterization.

This section addresses the details of the data, software, and attributes used to perform this research. The multicomponent seismic was recorded by the RCP in 2003 and processed by CGGVeritas. The well data and most of the wells logs were provided by Williams Production Co. The RCP collected the recent image and cross-dipole sonic wells logs. The analysis, S-wave splitting processing, and interpretation were done in Transform Software, Kingdom SMT, and Landmark software packages.

1.2.1 RCP Multicomponent Seismic

The RCP multicomponent seismic surveys in Rulison Field are 9-component seismic surveys and dedicated time-lapse surveys. Their similar acquisition and processing steps make them extremely repeatable, and Donald Keighley (2006) and Michael Rumon (2006) completed time-lapse seismic studies monitoring reservoir changes due to well production. This research uses the first or baseline survey acquired in November 2003 and focuses on the S-wave volumes. The specific volumes that this research uses are the post-stack migrated P-wave volume and the fast (S1) and slow (S2) S-wave volumes. The results presented in this thesis are primarily from the S1 and S2 volumes. S1 and S2 or fast and slow S-waves are define in detail in section 1.2.3

1.2.2 Seismic Design & Acquisition

The RCP seismic surveys cover a densely drilled area of Rulison Field shown in figure 1.10. This area, just north of interstate 70, has over 80 wells and an active drilling program at 10 acre spacing. The 2003 survey was recorded in October during very dry conditions. The survey covered an area of two square miles or, more precisely, 7260 feet by 8250 feet with 709 source points and approximately 1500 receivers. Inline receiver

spacing was 110-feet., and crossline receiver spacing was 330. Source spacing was 110-ft inline and 660-ft crossline with the source lines perpendicular to the receiver lines (Figure 1.8). This recording geometry was processed into 55-ft by 55-ft bins with 138 inlines and 152 crosslines.

All receivers were active for every source location allowing high fold, offset, and azimuthal distribution. Figure 1.9 shows a fold map for all offsets of the survey. The fold of the survey is highest in the center of the survey with a maximum fold of 225 (figure 1.9). Figures 1.8 and 1.9 show that the northern part of the survey has decreased fold due to decreased source and receiver locations. This is caused by steep and variable terrain in the northern area associated with the base of the Roan Plateau. The areas with lower fold have proportionally lower signal to noise ratios and, therefore, are less reliable. The edges of the survey were trimmed for the S-wave splitting calculations. 20 lines were trimmed from the east and west edges, 30 lines from the south edge, and 40 lines from the north. Trimming resulted in a focus on only the high fold center part of the survey and eliminated much of the error that low fold data would introduce into the calculations. Data were not trimmed for the basic fault interpretations.

Solid State Geophysical acquired the survey for RCP with vibroseis sources. The P-wave source was an AHV-IV 62000 lb vibrator which conducted six 5-120 Hz 10 second sweeps at each source point. The S-wave source was a mix of IVI Tri-AX and Mertz 18 shear vibrators with two horizontal sources. The shear vibrators swept from 5-50 Hz during a 10 second period 6 times per source location. The receivers were I/O VectorSeis® System Four™ single sensor digital (MEMS) receivers. The receivers were GPS surveyed into place to assure maximum repeatability. These receivers were planted

singularly at each receiver location and compass oriented into uger-drilled holes to assure maximum coupling. The receivers recorded for 16 seconds, and the receiver sampling rate was 2-ms with an instantaneous dynamic range of 118 dB. (I/O, 2005). Table 1.1 summarizes the survey parameters discussed in this section.

Table 1.1 Survey acquisition parameters (Jansen, 2005).

Survey Location	Rulison Field, Piceance Basin, Colorado (T6S R94W)
Survey Type	4-D, 9-C
Survey Size	7260’ X 8250’ (2.15 mi^2)
# Receiver Locations	~1500
# Source Locations	~700
Receiver Grid	110’ inline spacing, 330’ between lines
Receiver Type	VectorSeis® System Four™ digital single sensor (MEMS)
Receiver Sampling	2 ms
Source Grid	110’ inline spacing, 660’ between lines
Source Type	Vibroseis
Source P-wave	Mertz 18
Source S-wave	IVI TRI-AX/Mertz
P-wave Sweep	6-120 Hz for 10 seconds 6 times per location
S-wave Sweep	5-50 Hz for 10 seconds 6 times per location

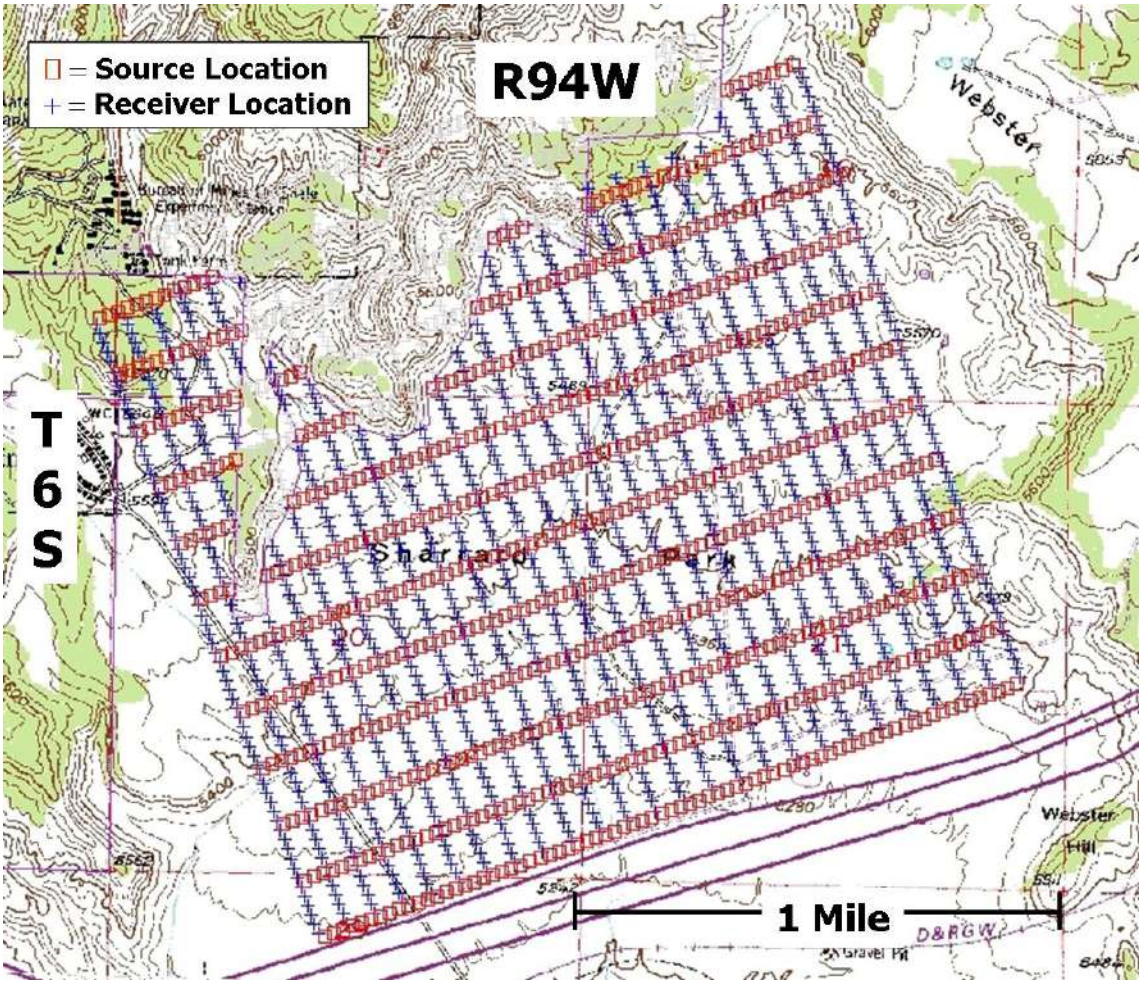

Figure 1.8. A topographic map of the RCP survey area at Rulison Field showing source and receiver locations and the spatial extent of the survey.

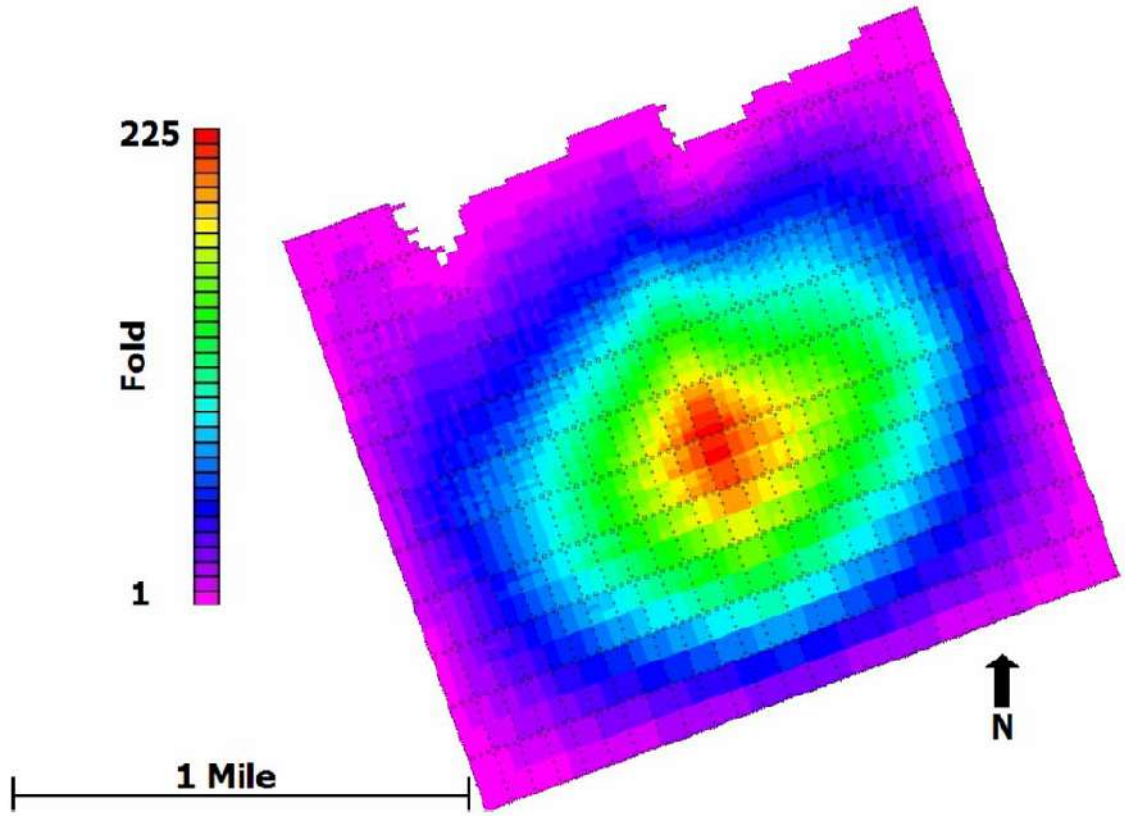

Figure 1.9. Fold Map of the RCP survey (Rumon, 2006).

1.2.3 Seismic Processing

Veritas DGC in Calgary (now CGGVeritas) processed the P-wave and S-wave seismic data. Table 1.2 shows the processing sequence for the P-wave data, and table 1.3 shows the processing sequence for the S-wave data. The seismic data were post-stack Kirchoff migrated.

The fundamental difference between an S-wave and a P-wave is the direction of particle motion. The particle motion of an S-wave is orthogonal to the direction of propagation, whereas, the particle motion of a P-wave is parallel to the direction of propagation. The consequences of this difference must be accounted for in an extra S-wave specific processing step known as an Alford rotation. This step is required in S-

wave processing because of a phenomenon known as S-wave splitting. An S-wave propagating through an isotropic medium will move with the S-wave velocity of the medium and will maintain the particle motion polarization of which the wave entered the medium. If an S-wave enters an anisotropic medium, such as a medium with aligned fractures, it will immediately split into two waves if the initial polarization is not parallel or perpendicular to the fractures (Thomsen, 2002). Figure 1.10 demonstrates this phenomenon by showing how S-waves with a variety of polarizations split and change velocity and polarization when entering an anisotropic medium. As the figure shows, an S-wave not parallel or perpendicular to the fractures will split into an S-wave polarized parallel to the fractures that moves with the S-wave velocity of the medium and an S-wave polarized perpendicular to the fractures that moves with a slower velocity. The S-wave that is parallel to the fractures is referred to as S1, and the S-wave that is perpendicular to the fractures is referred to as S2.

Table 1.2. P-wave seismic processing sequence

1. Tilt correction for Vectorseis phone applied in the field
2. Demultiplex/Geometry/First Break Picks
3. Refraction Tomography Statics
4. Manuel Trace Edits/Amplitude Recovery – T2
5. Surface Consistent Amplitude Equalization
6. Surface Consistent Deconvolution
7. Velocity Analysis (Preliminary)
8. Surface Consistent Statics (Preliminary)
9. Velocity Analysis
10. Surface Consistent Statics
11. First Break Mutes
12. Trim Statics
13. Amplitude Equalization – Mean Scaling
14. Stack
15. Noise Attenuation (Fxy Deconvolution)
16. Migration - Kirchoff
17. Filter – 5/10-100/110Hz 0-1600ms, 5/10-80/95Hz 1600-2800ms
18. Amplitude Equalization – Mean Scaling

Table 1.3. S-wave seismic processing sequence

1. Tilt Correction for Vectorseis phone applied in the field
2. Demultiplex
3. Geometry Correction
4. Manuel Trace Edits
5. Polarity Correction – Receiver and Shot
6. Spherical Divergence Correction
7. Surface Consistent Amplitude Equalization
8. Alford Rotation – N43W
9. Minimum Phase Correction
10. Surface Consistent Deconvolution
11. Source/Receiver Statics – From P-S Data
12. CDP Gather
13. Velocity Analysis (preliminary)
14. Noise Attenuation – Radon Transform
15. Surface Consistent Statics (Preliminary)
16. Velocity Analysis
17. Surface Consistent Statics
18. First Break Mutes
19. Trim Statics
20. Amplitude Equalization – Mean Scaling
21. Stack
22. Noise Attenuation (Fxy Deconvolution)
23. Migration - Kirchoff

Alford rotation rotates the data recorded by the two orthogonal components in the survey coordinate system to the S1 and S2 coordinate directions. If the survey coordinate system is already aligned with the fracture anisotropy, this step would not be necessary as we would excite and record the S1 and S2 separately on the two horizontal components of the geophone. Since our survey coordinate system is not aligned with the anisotropy coordinate system, the source S-wave splits and both receivers record the S1 and S2 components. This creates a matrix of crossline and inline sources and receivers containing energy from both S1 and S2 polarizations (figure 1.11). The Alford rotation concentrates the energy along the diagonal principle component of the matrix through a tensor rotation to the direction which the S1 and S2 energy is maximized and the energy in the off-diagonal directions is minimized (Alford, 1986). This rotation allows the S1 and S2 data to separate and shows the principle direction of azimuthal anisotropy (Thomsen, 2002).

An Alford rotation to an azimuth of 317 degrees was applied to the Rulison 9-component data. This angle resulted in the largest minimization of off-diagonal energy. This angle is similar to the polarization angle calculated from the 2003 VSP data obtained in well RMV 30-21 which was N46W.

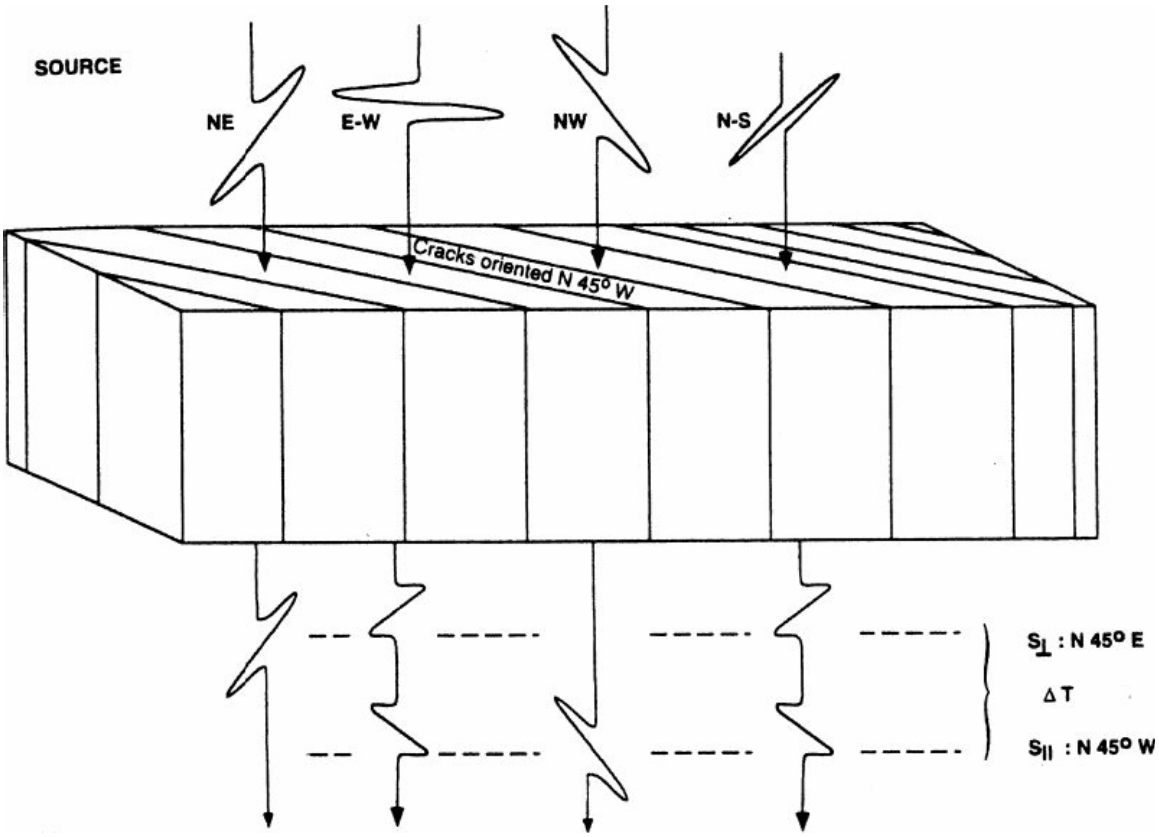

Figure 1.10. Diagram showing S-waves of various polarizations entering a fractured anisotropic medium. S-waves polarized obliquely to the fractures split into two S-waves. S-waves polarized parallel or perpendicular to the fractures do not split and continue to propagate with there initial polarity. (Sheriff and Geldart, 1995)

Inline Receivers Inline Sources	Crossline Receivers Inline Sources
Inline Receivers Crossline sources	Crossline Receivers Crossline Sources

Figure 1.11. Matrix used to produce rotated data (modified from Rumon, 2006)

1.2.4 Well Data

This research uses existing well data from the RCP survey area to evaluate the validity of the seismic interpretations. Williams Production Company provided the majority of the well data, and the RCP provided some of the image and cross-dipole sonic logs. The well data that this research uses are estimated ultimate recovery (EUR) values calculated from well production, and image, cross-dipole sonic, and gamma ray logs from the eight key wells in the high fold area. Figure 1.12 shows the location and EUR values of many of the wells in the field overlain on the seismic fold map. Notice the range in EUR values between closely spaced wells. Figure 1.13 shows the selected eight wells and high fold area of the survey. These wells were selected because they are located in the high fold section of the survey and have image and sonic logs or exceptionally high or low EUR values. The red wells have EUR values greater than 2.5 BCF (wells H1, H2, and H3), and the green wells have EUR values of 1.0-1.5 BCF (wells L1, L2, and L3). The purple wells have image and cross-dipole sonic logs (wells W1 and W2).

The image log interpretation for faults and fractures of wells W1 and W2 were done by Marin Matesic (Matesic, 2006) and Halliburton (Hargrow, 2006), respectively. The anisotropy logs were calculated as the percent difference between the rotated fast and slow S-wave logs from cross-dipole sonic logs. This research uses the fault and fracture interpretations and anisotropy calculations from these logs as ground truth to verify seismic interpretations.

1.3 Work Flow

The research presented in this thesis can easily be divided into two sections. The first section, which is presented in chapter 2, addresses the approach, analysis, and results of

reservoir level fault detection from S-wave seismic. The second section, which is presented in chapter 3, investigates and tests new techniques for S-wave splitting analysis that are applicable to thick tight gas sand reservoirs.

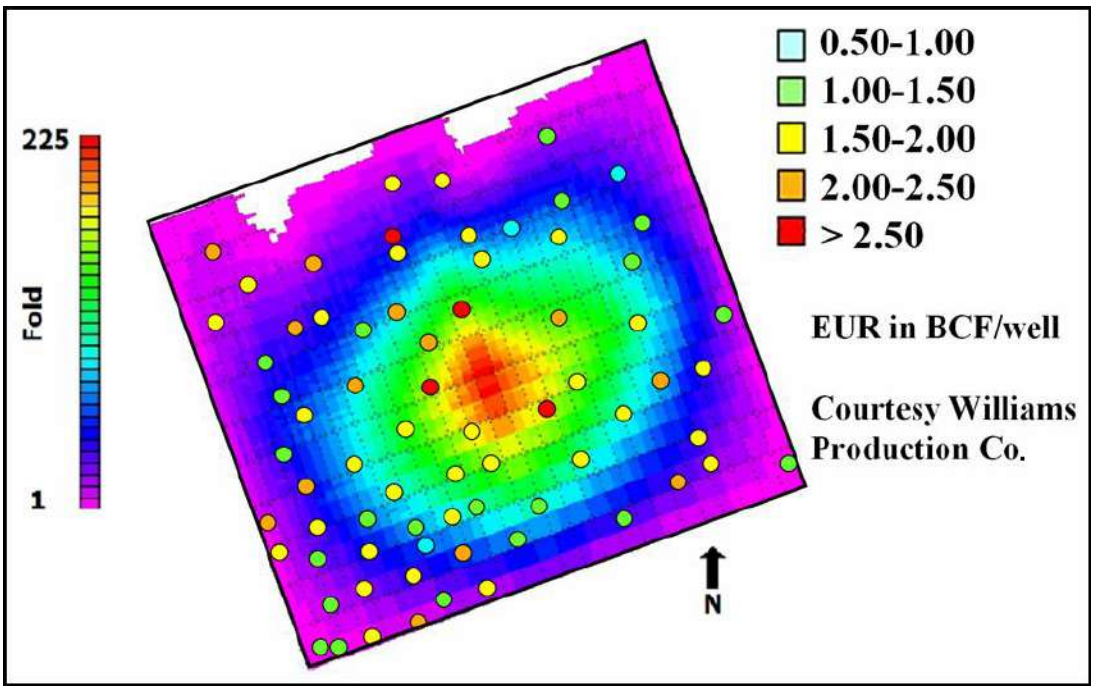

Figure 1.12. Locations of wells in the RCP seismic survey with EUR data colored by EUR values (modified from Rumon, 2006)

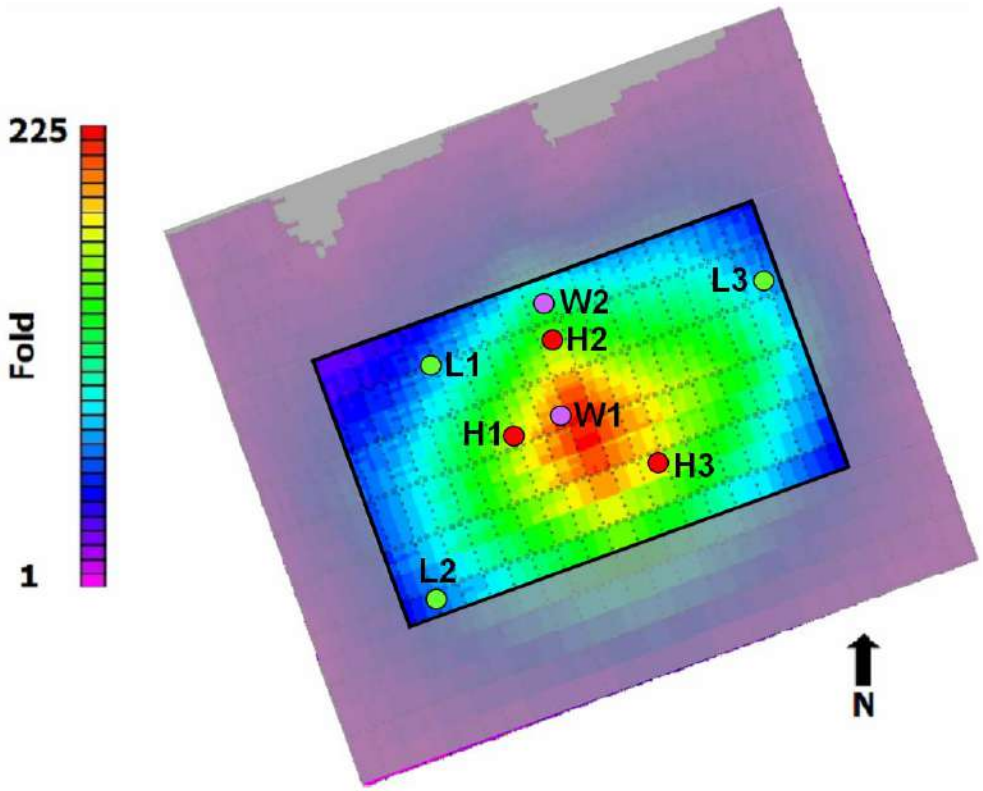

Figure 1.13. High fold area of the seismic survey and wells used for in this research (modified from Rumon, 2006)

CHAPTER 2 FAULT DETECTION FROM S-WAVE SEISMIC

S-wave seismic is not conventionally used for fault interpretation. P-wave seismic is typically used for basic structural interpretations because it is cheaper than S-wave seismic to acquire and simpler to interpret. In many geologic environments P-wave seismic provides an adequate structural image, but P-wave seismic struggles in the tight gas sand reservoir of Rulison Field. S-wave seismic in the RCP study area provides a more robust image of reservoir level faults. The research presented in this chapter explains how my fault interpretation from the RCP S-wave seismic was completed and the results of this interpretation along with the geologic significance of these faults.

Jackson (2007) and others have published fault interpretations in the basin-centered gas accumulation area of the Piceance Basin. There are two significant differences between these past interpretations and my interpretation. The first difference is that most of the previous research has focused on basin-scale to field-scale interpretations that showed little interpretable faulting in the reservoir rock. This appears to be primarily due to lack of reflector continuity in the P-wave seismic throughout most of the reservoir interval. My interpretation focuses on the reservoir interval of the high fold RCP survey and is of smaller scale and higher resolution than the other studies. The other difference is that all previous interpretations used P-wave seismic, and most used the 2001 Seitel P-wave seismic survey which has lower spatial resolution and fold than

the RCP survey. A final difference is my tie to well observation of faulting by tying my work to that of Matesic (2006).

2.1 Previous Interpretations

Several regional and field scale fault interpretations of the Piceance Basin have been published in recent years. Two of the notable interpretations of the Rulison field area are studies by Cumella and Ostby (2003) and Jackson (2007). Both of these structural interpretations were made primarily from well data and the 2001 Seitel P-wave seismic survey that covers much of Parachute and Rulison Field.

Cumella and Ostby (2003) interpreted the central Piceance Basin to have an overall left-lateral transpressional structural style caused by Laramide east-west compression. Figure 2.1 shows an outline of the Seitel survey and the interpreted Rollins level faults and time structure map from Cumella and Ostby (2003). Most of the interpreted faults strike northwest to north-northwest. Cumella and Ostby interpreted the faults striking to the northwest to have left-lateral slip and very little vertical offset. Most of the faults trending to the north-northwest show reverse motion and have dips between 30-60 degrees. Figure 2.2 shows the seismic section from the location of the green line in figure 2.1. The seismic line shown in figure 2.2 illustrates that most of the faults shown in figure 2.1 are deep-seated faults propagating up from well below the Mesaverde Formation. This figure also shows how the faults appear to die out at the reservoir level above the Cameo Coals. Cumella and Ostby indicated the faults splayed, bifurcated, and died out into the Williams Fork and left the Upper Mesaverde relatively unfaulted. They also suggested that natural fractures in the Mesaverde are likely to be related to the splaying of these deep-seated faults and located near the splays.

Jackson (2007) presented a detailed structural model of Rulison Field that shows primarily reverse faults that trend in a NW direction. His thesis gives a detailed structural history of the Rulison Field area of the Piceance Field. He also calculates the stress, offset, and nearby fracturing of the major faults which he uses to relate to reservoir connectivity and compartmentalization. Few of his seismically interpreted faults extend into the reservoir, and most of the faults that he uses in his interpretation are large scale, planar, low angle, deep seated, reverse faults. These faults are very important to general field-scale reservoir characterization. However, my focus is on the more subtle reservoir level faults that directly affect the rock properties seen in the Williams Fork Formation above the Cameo Coals.

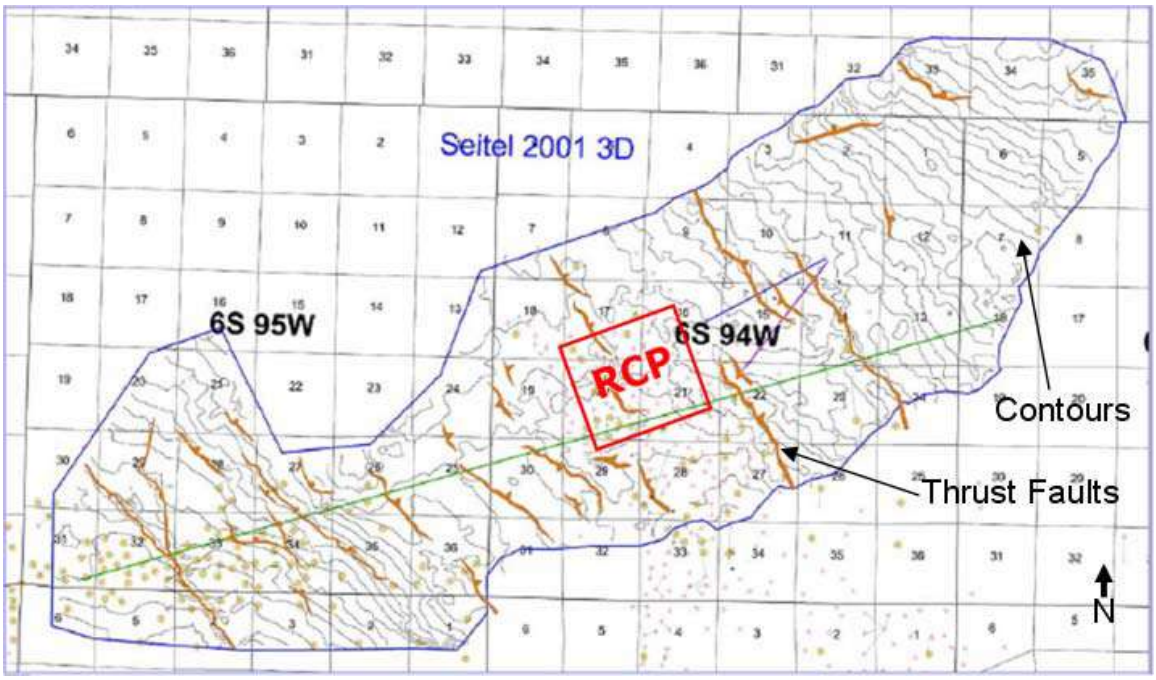

Figure 2.1. The outline of the Seitel seismic survey is shown in blue, and the outline of the RCP survey is shown in Red. A time structure map and interpreted faults at the Rollins horizon are shown inside the Seitel survey. Most faults are reverse faults with a northwest strike (modified from Cumella and Ostby, 2003).

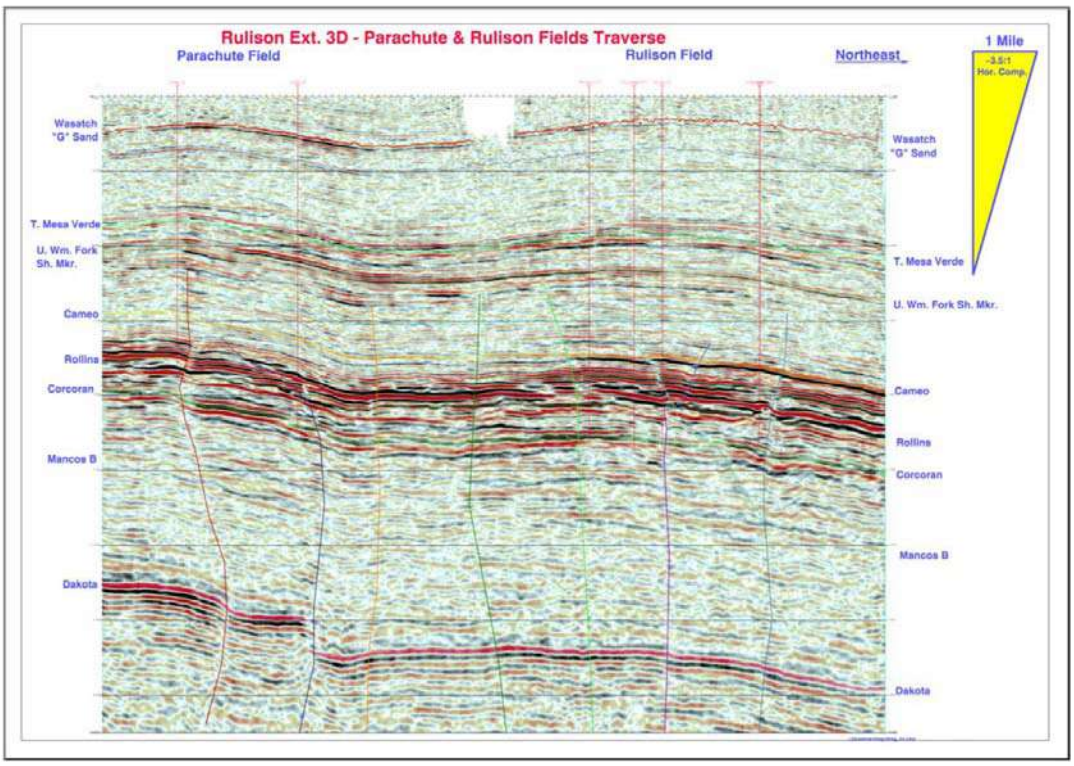

Figure 2.2. Seismic line from the Seitel survey from Parachute to Rulison Field showing the interpreted faulting. Faulting is evident below the Cameo horizon but not above in the reservoir rock. The location of this line is shown in figure 2.1 by the green line. (Cumella and Ostby, 2003)

2.2 Methodology

My fault interpretations follow conventional P-wave interpretation methodology with the exception that I used S-wave seismic. The first step of my interpretation process was to prove that the S-wave seismic volumes were the best volumes in the RCP dataset to use for structural interpretation. I started my initial analysis by qualitatively comparing the structural imaging of the RCP P-wave, converted-wave, and S-wave data sets. Figure 2.3 shows trace 80 from the P-wave, converted-wave, and S-wave datasets. This figure shows consistent reflectors near the top of the reservoir (UMV Shale) and in the lower reservoir (Cameo) in all datasets, but this figure also shows the very different reflectivity seen between these two horizons in the datasets. This figure illustrates the differences between the elastic and acoustic response of the reservoir rock. The P-wave seismic line

shows that the main horizons can be interpreted, but that there is very little interpretable signal in the reservoir. The vertical seismic line through the S-wave data shows continuity of offset reflectors and reflection dimming. These are the types of features that would indicate faulting that I have interpreted as faults from the S-wave data.

Next, I created coherency-type volumes and surfaces from the initial volumes to help better detect and resolve structural features. The converted-wave data were eliminated from this analysis at this point due to lack of interpretable structural features caused by the apparent low signal to noise ratio. The initial coherency-type comparison was created by the Landmark Software's PostStack Pal's 'ESP Along a Horizon' algorithm. These attribute maps were created from a time window centered on the horizon. The centered time window used for the P-wave seismic is 25ms, and the centered time window used for the S-wave seismic 50ms. The window length was doubled for the S-wave data since typical S-waves velocities are half the velocity of P-waves; the time window is between half of a wavelength and one wavelength for both datasets. Figure 2.4 shows these attribute maps at the Cameo horizon for the P-wave and the S-wave seismic. The S-wave attribute map reveals semi-linear discontinuities that coincide with interpretable faults caused by reflector offset or dimming in vertical seismic sections. The P-wave attribute map also has areas of high discontinuity, but these areas in the center of the survey do not have a typical faulting configuration and do not tie to any sort of apparent seismic faulting. Interpretations of the Seitel P-wave seismic show a major fault at this western edge of the RCP survey (Jansen, 2005). This fault is not seen in the S-wave figure because of the low fold and signal-to-noise ratio at the edge of the survey. From comparison of the high fold area of two horizon slices shown in

figure 2.4 and similar comparisons on other horizons below the reservoir and above, I concluded that the S-wave data detected structural features better than the P-wave. The S-wave attribute map in figure 2.4 provided the basis for my fault interpretation. Two faults can be seen striking to the north-northwest through the middle of the survey. One is a deep fault and the other is a splay from the first fault that initiates in the lower Cameo Coals.

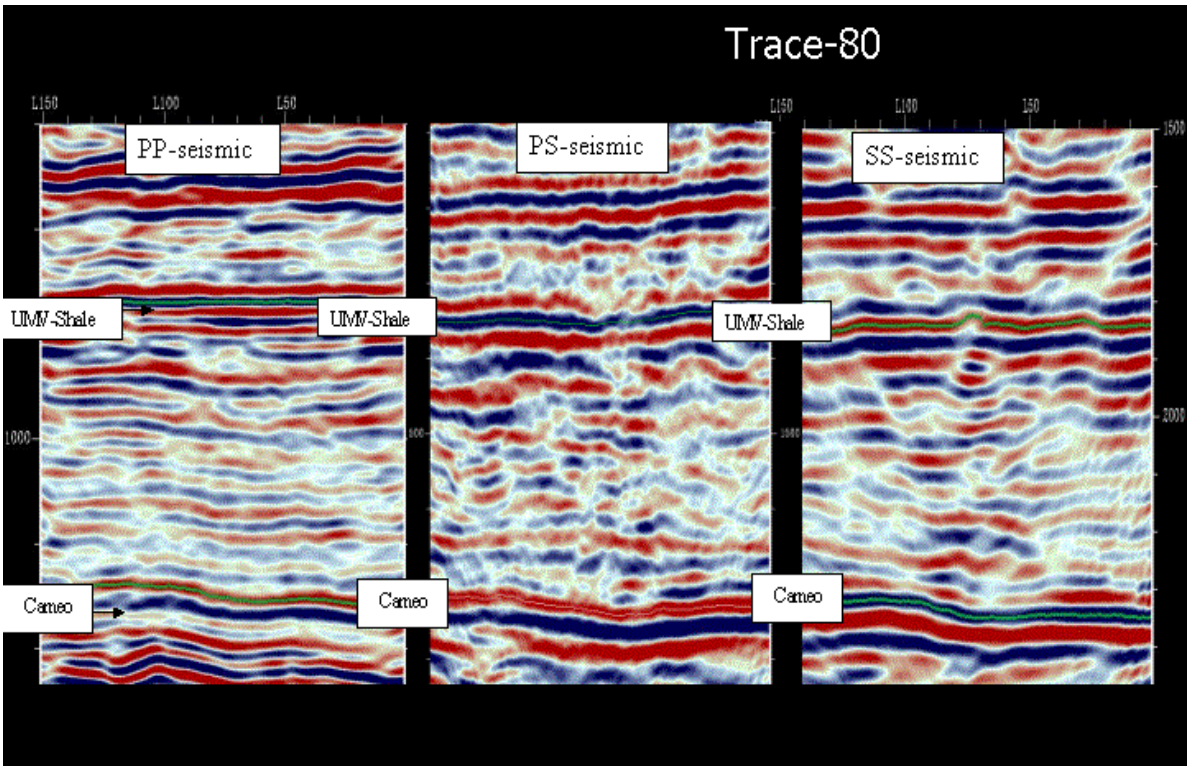

Figure 2.3. Trace 80 from the RCP dataset showing the P-wave (PP), converted-wave (PS), and the S-wave (SS) vertical seismic data. (Davis, 2005)

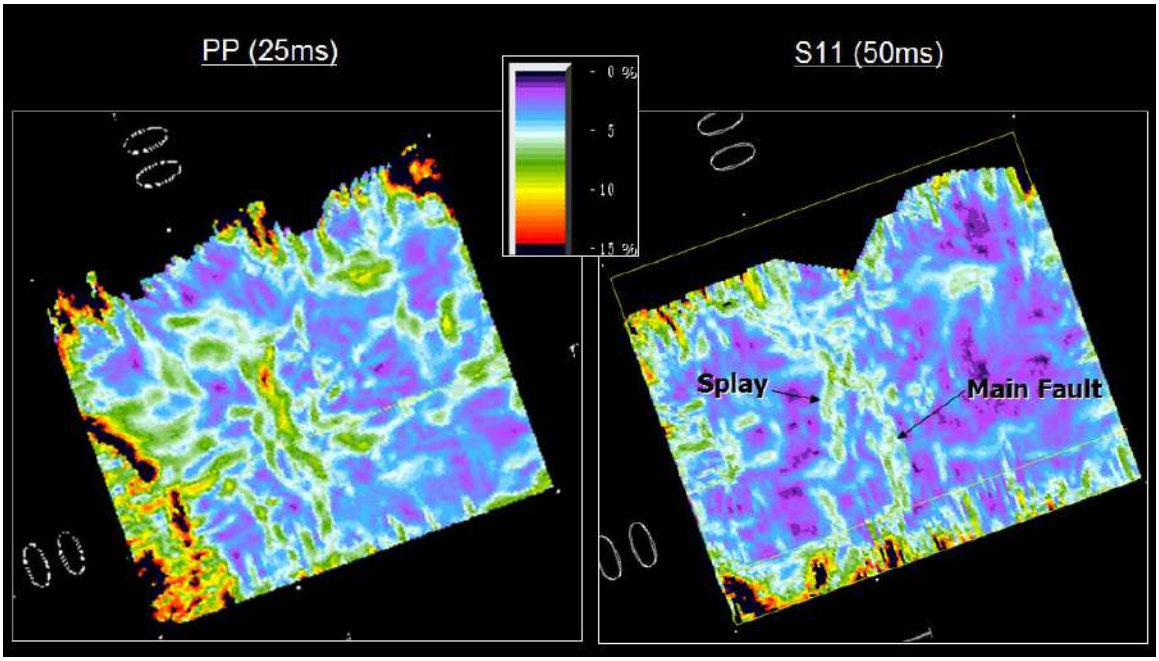

Figure 2.4. Coherency-type horizon-based attribute of the Cameo horizon. The purple and blue areas are coherent areas; the white to green areas are incoherent areas where faulting might exist. Shear-wave attribute maps shows linear trends that might be faults that are not apparent on the P-wave map.

Coherency-type volumes were created to look beyond the horizon-based data. The similarity algorithm in Transform Software's TerraMorph^{TM} package created coherency-type volumes for the S1, S2, & P-wave seismic. This algorithm is a proprietary seismic attribute that compares the change in frequency and amplitude from the input trace to the surrounding traces. The algorithm has two user inputs: window length and number of traces to compare. The inputs I used for the S-wave volumes were a window length of 64ms and 8 traces to compare, and the inputs I used for the P-wave volume were a window length of 36ms and 8 traces. The S-wave similarity volumes revealed discontinuities consistent with the discontinuities seen in the S-wave horizon attribute map shown in figure 2.4.

I used time slices of these attribute volumes and the base S-wave seismic in vertical trace display to make my detailed reservoir interval fault interpretations. I also

evaluated curvature volumes to help with the interpretation, but ultimately did not use curvature. The volume curvature algorithm as I applied it did not reveal structural features with any consistency. My interpretation focuses on the north-northwest trending fault near the center of the survey that is labeled 'main fault' on figure 2.4. I focused on this area because this fault and the splay shown in figure 2.4 are located in the high fold area of the survey. A central fault and its associated splays were hand picked in Kingdom™ software on depth converted S1 and S2 seismic and similarity attribute volumes. The actual fault planes were picked on depth slices starting below the reservoir at the Rollins sandstone horizon and moved up through the reservoir at 50ms increments to the UMV Shale reflector which encompasses the reservoir. This procedure resulted in four main fault planes that are non-planar. These fault planes were then compared to known faults and fracture zones from well logs and well production data to identify correlations between seismically interpretable faults and image log faults and well production.

2.3 Interpretation

The main fault and the three fault splays interpreted using the procedure detailed above are interpreted strike-slip faults that create strike-slip splays. Strike-slip splays occur at bends of strike-slip faults. The rock within the bend becomes progressively faulted due to the change in strike of movement along the main fault. These structures are often described as flower structures because of their steeply dipping fault splays that connect at depth to the main fault and diverge upward. Depending on the direction the fault is moving and the direction of the bend, these structures will either be compressional or extensional flower structures (Davis and Reynolds, 1996). The

interpreted reservoir level faults best fit the structural model of a compressional flower structure. Figure 2.5 shows a cross-section and 3-D diagram of a compressional flower structure. This figure shows that even though the main movement on the faults is along strike, there can also be reverse movement.

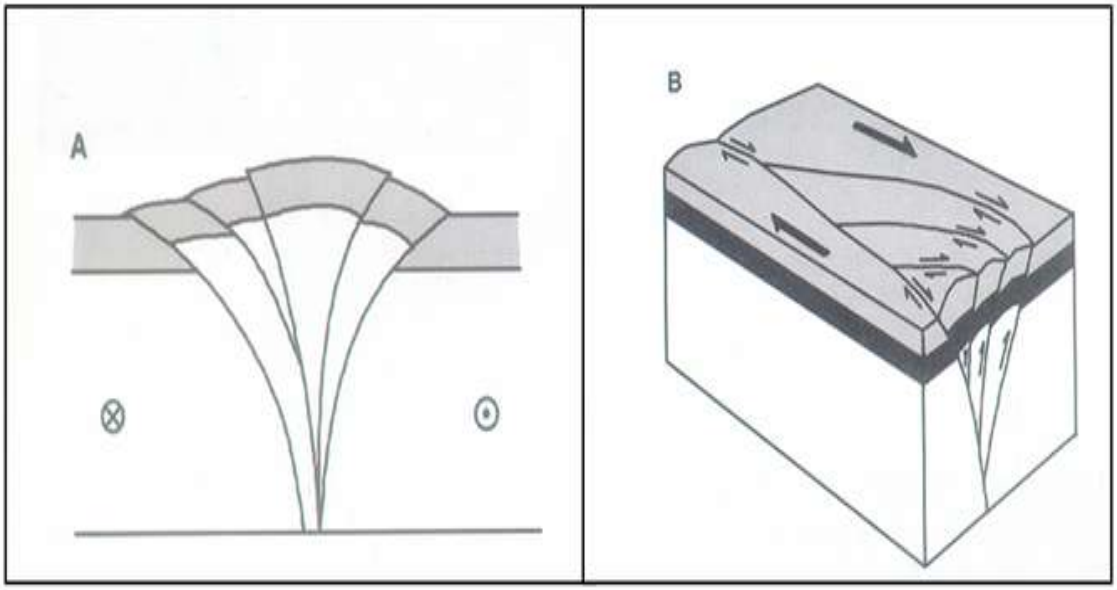

Figure 2.5. A) Compressional flower structure or palm tree structure in cross-section. B) Diagram showing how palm tree structures form at bends in strike-slip faults. (Davis and Reynolds, 1996)

Figure 2.6 shows a depth slice below the Cameo Coal horizon from the S1 & S2 similarity volumes. The S1 similarity volume is displayed with a blue-white scale, and the S2 volume is displayed with a red-white scale. The red or blue areas are where the similarity algorithm detected dissimilar traces. Where these areas create semi-linear features that coincide with discontinuities in the vertical seismic displays, I interpreted a fault. Figure 2.7 shows my interpreted fault traces on the same depth slice as figure 2.6. In the Cameo Coals these faults are visible in the seismic, but as many of them splay upward through the reservoir, they become below seismic resolution and cannot be interpreted.

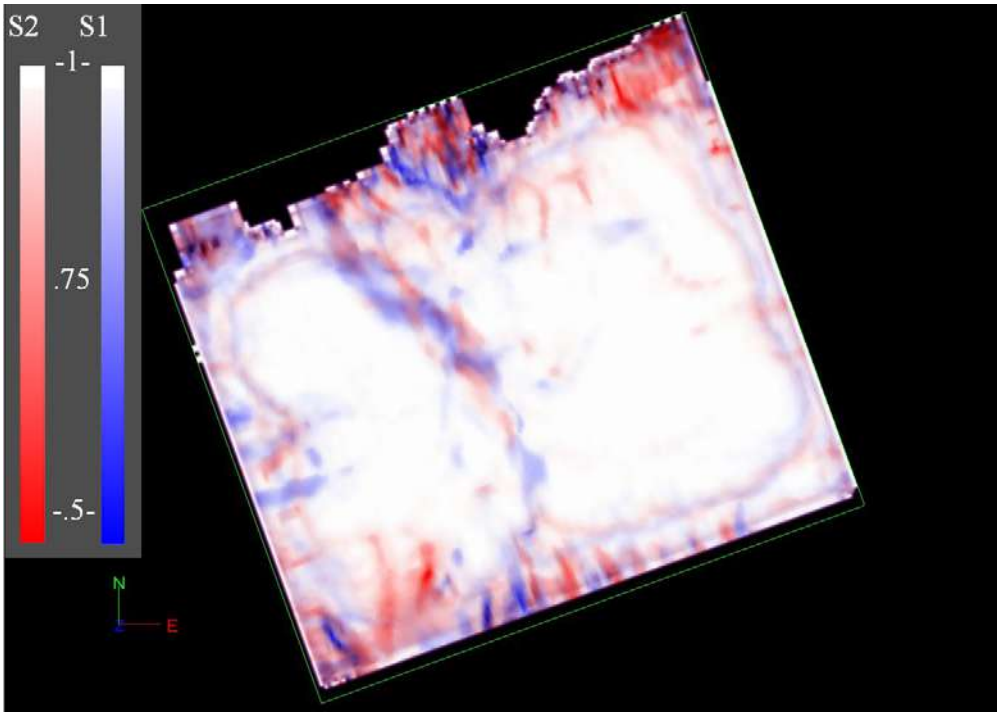

Figure 2.6. Co-rendered depth slice of the S1 & S2 similarity volumes slightly below the Cameo horizon. S1 is displayed with a red scale, and S2 is displayed with a blue scale.

Figure 2.8 shows a map view of the four fault planes that were interpreted through the reservoir. These faults are shown propagating upwards above the Cameo horizon in the lower reservoir of the S1 similarity volume. These four fault planes can be seen in a 3-D view in figure 2.9. Three of these faults are also shown in vertical display in figure 2.10. The vertical display shows the basic seismic data in black and white and the similarity volume on a color scale. The yellow, pink, and green fault traces correspond to the fault planes in the previous figure. This figure demonstrates the types of events that were interpreted as faults. There are other anomalous events on this line that resemble faulting, but these events could not be followed through the rest of the seismic volumes so they were not interpreted as faults.

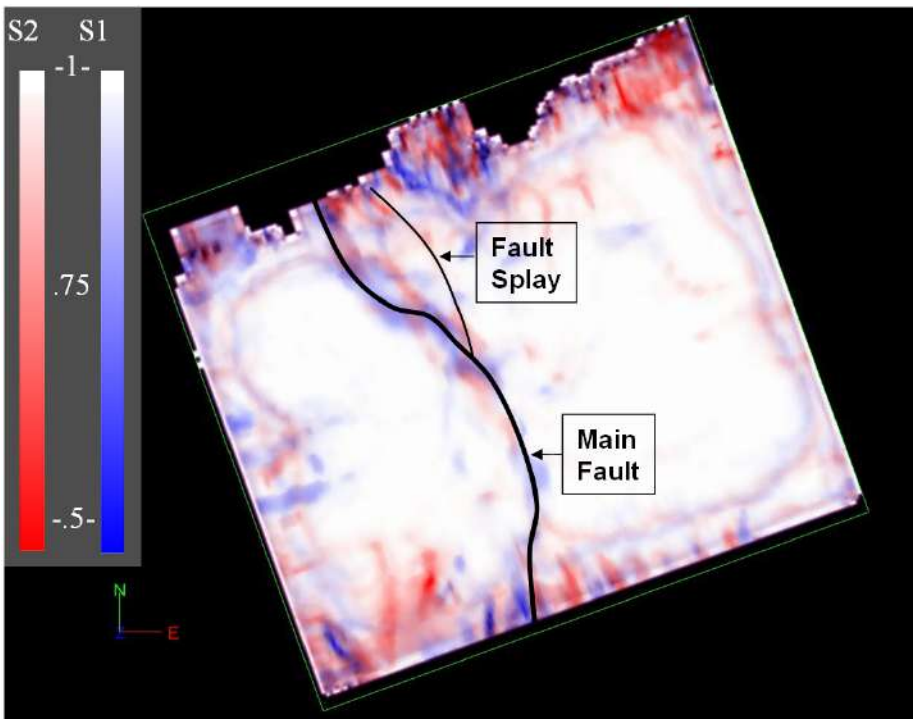

Figure 2.7 The same depth slice shown in figure 2.6 with interpreted fault

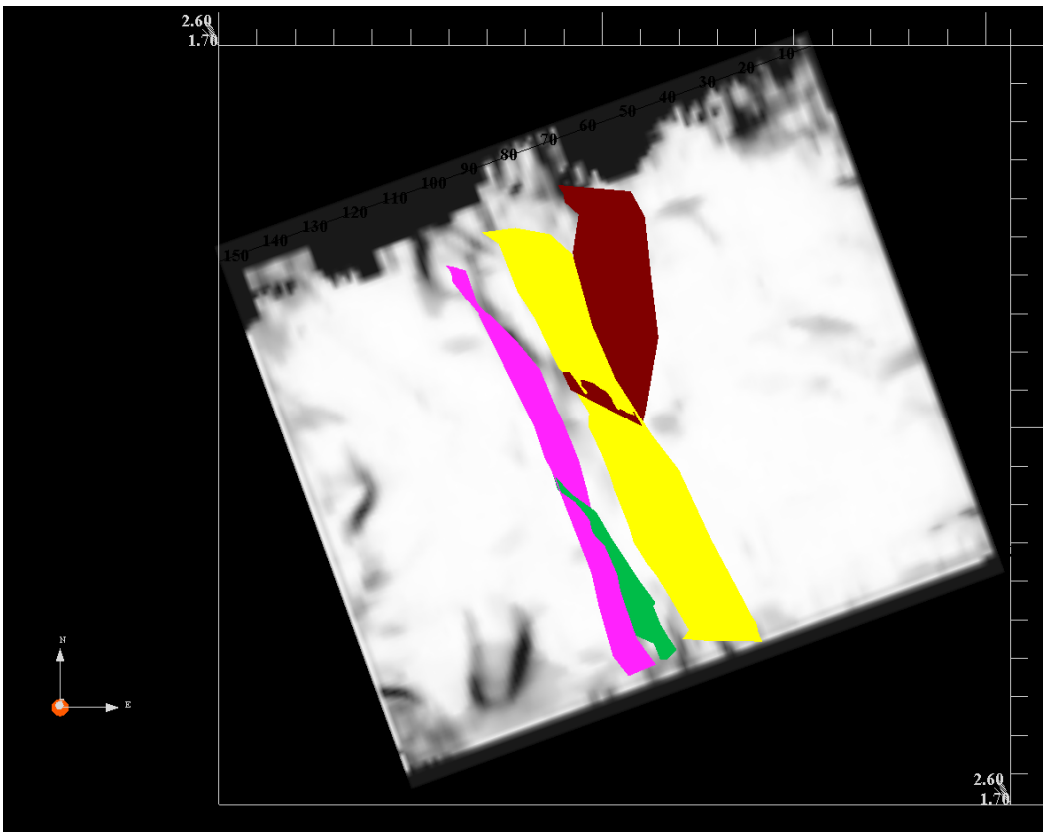

Figure 2.8. Map view of the interpreted 3-D faults planes intersecting a depth slice of the S1 similarity volume above the Cameo horizon.

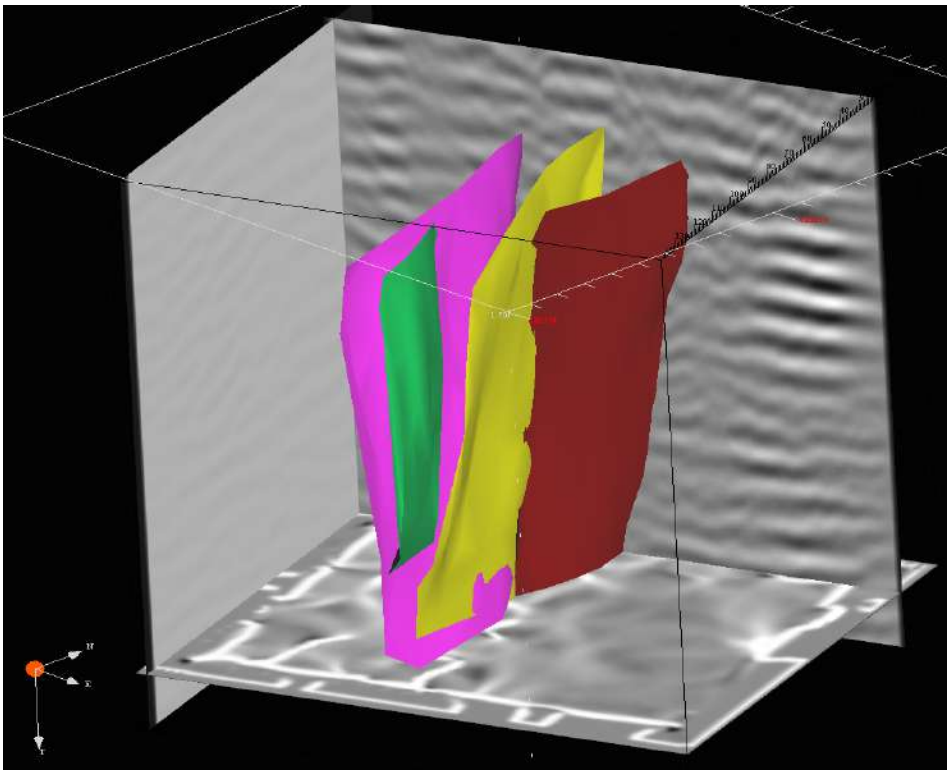

Figure 2.9 3-D faults planes from the original Cameo level fault.

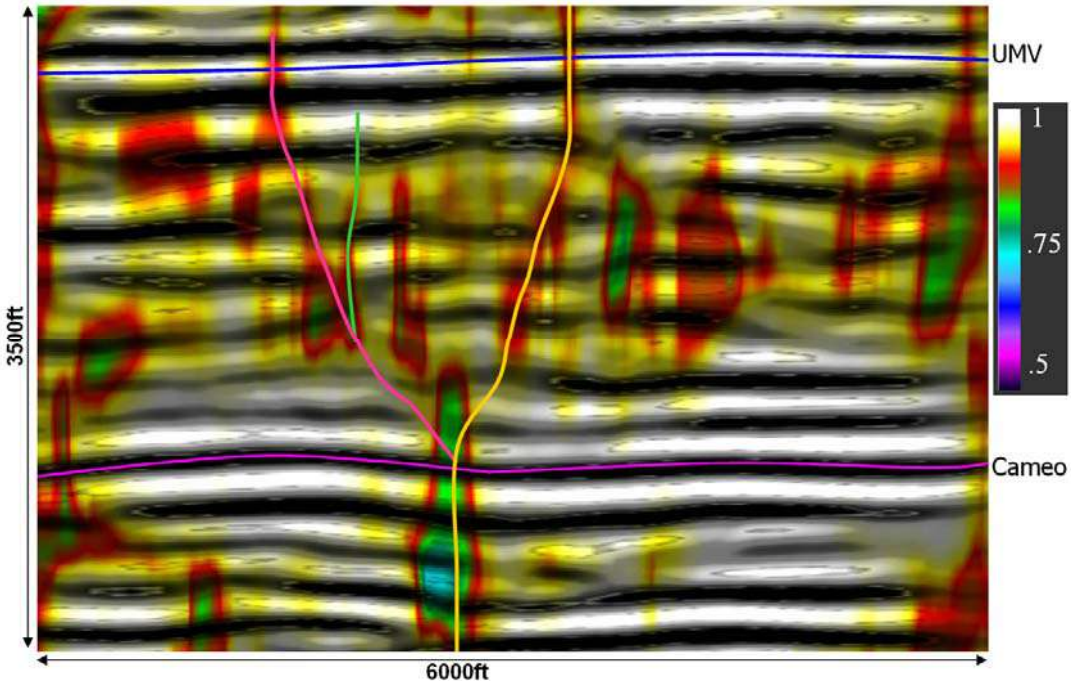

Figure 2.10 Approximate E-W seismic line in the south part of the survey (crossline 100) showing the base S1 seismic in black and white with the S1 similarity volume in a color scale. Three of the fault planes are shown. Areas that are very similar have a value near 1 and are shown as white; areas that are dissimilar have values less than 1 and are shaded by value according the colorbar.

The yellow fault is the main strike-slip fault. This fault strikes to the north-north west and is near vertical with a slight dip to the west. The red fault is a splay that separates vertically from the main fault below and through the reservoir and strikes more northerly than the main fault. The pink fault is a splay that separates horizontally from the main fault above the Cameo horizon and dips to the east but maintains a similar strike to the main fault. The green fault separates horizontally from the pink fault in the middle reservoir and strikes to the northwest.

There are likely many more fault splays associated with this strike-slip duplex that are below the resolution of the seismic. Many other possible faults were apparent in the seismic at different depths in the reservoir. I did not interpret these as faults since I could not trace them through more than a few depth slices. These faults may be below the resolution of the seismic to be able to confidently interpret. The faults that I interpreted are only the faults that I felt confident in picking throughout the reservoir.

2.4 Well Data Comparison

Since the RCP survey area has an abundance of well data, the best way to verify the existence and location interpreted fault planes is to compare these fault planes with known faults that have been interpreted in well logs. I also compare the faults with Expected Ultimate Recovery (EUR) data from the three best and worst wells in the field to see if there is any correlation between a well's production and proximity to faults. Figure 2.11 shows the four interpreted fault planes with the eight comparison wells that are discussed in section 1.2.4.

Wells W1 and W2 have image logs and cross-dipole sonic logs and are located in the high fold area of the RCP survey. The image logs in these two wells are used to verify

the seismic fault planes. The image log in well W1 was interpreted by Marin Matesic (2007), and the image log in well W2 was interpreted by Halliburton (Hargrow, 2006).

Figure 2.12 shows well W1 and the fault planes. This well only intersects the interpreted pink fault plane. Marin Matesic (2007) interpreted five faults in the reservoir interval from this well's image log. His interpreted faults are shown at their corresponding depths on the right edge of figure 2.12 as black lines on the left side of the depth track of the gamma ray log from well W2. Three of his interpreted fault cuts are in the middle reservoir within a few hundred feet of each other. This well cuts the pink fault plane approximately 50ft below the lowest of Matesic's mid-reservoir fault cuts. Matesic interpreted the fault above the seismic fault plane to have an azimuth of 338 degrees and a dip of 64 degrees. The pink fault plane has approximately the same azimuth and a slightly steeper dip than Matesic's fault cut. These faults are not at the exact same depth, but are likely the same fault. Time-to-depth conversions are difficult in tight gas sand environments especially with S-wave seismic so a 50ft shift is an acceptable error. This well tie verifies the existence of the pink fault plane near well W1.

Well W2 cuts the yellow fault in the upper reservoir and the red fault in the middle area of the reservoir (figure 2.13). Well W2 intersects the yellow fault in the upper portion at approximately 5600ft. This is the depth that Halliburton has interpreted mineralized natural fractures striking in the same direction as the interpreted fault (figure 2.14). The anomalous mineralized fractures are circled in green on figure 2.14. These fractures have the same strike but have a much shallower dip and dip in the opposite direction of the fault. There are also many open natural fractures interpreted by Halliburton at this depth (figure 2.15). One of these natural fractures has a northwest

trend. After careful review of Halliburton's fracture interpretations on the image log, I have concluded that the open natural fracture at 5625ft that strikes to the northwest with a dip of about eighty degrees to the west is actually a small offset fault. The existence of this fault is also substantiated by the dense mineralized and open natural fractures at this depth.

This well also intersects the red fault in the lower reservoir. The image log does not show conclusive evidence of this fault. However, Riley's (2007) research on microseismic in this area detected a fault near the location of the red fault plane at this depth near well W2. The existence of the green fault plane cannot be confirmed because none of the wells with image logs cut the fault and faults cannot be detected on traditional logs.

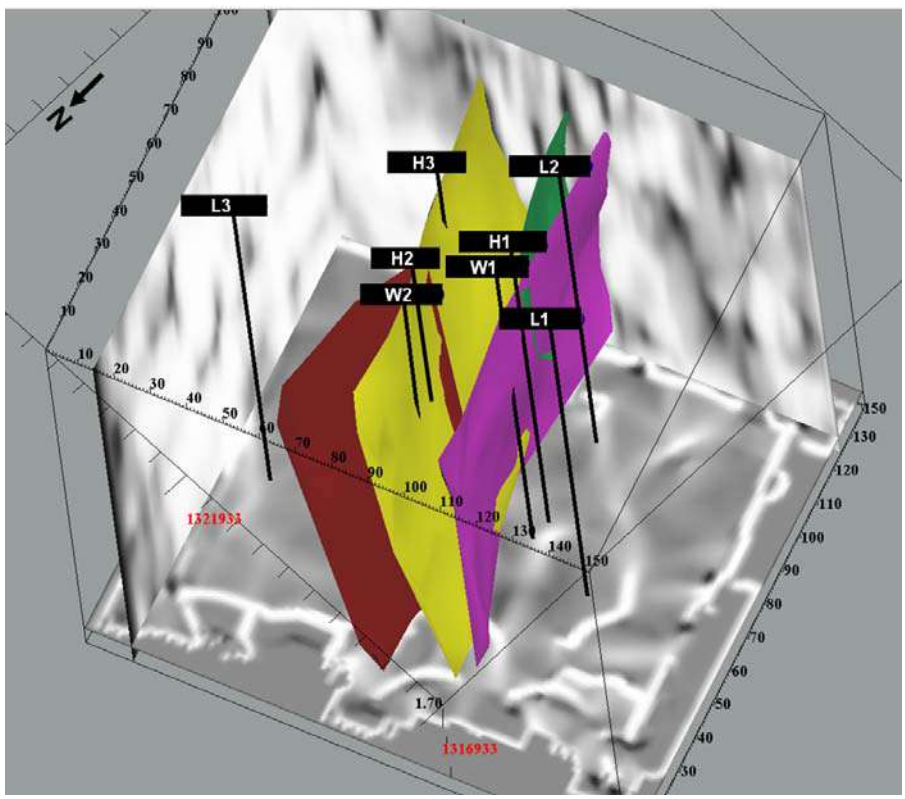

Figure 2.11. The fault planes shown with the comparison wells. The survey has been rotated approximately 180 degrees to better show the locations of the correlation wells.

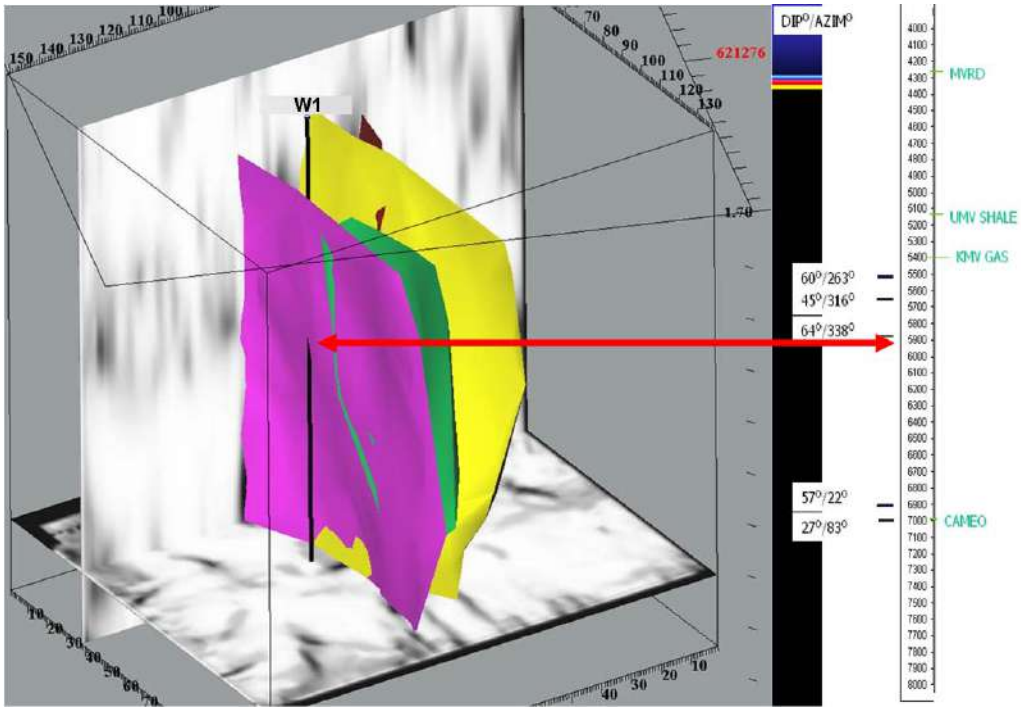

Figure 2.12. The fault planes shown with Well W1. The pink fault plane intersects well W1 at approximately 5950ft which is just below Matesic's interpreted fault cut from the image log of 5880ft. (Well log image on the right side from Matesic, 2007)

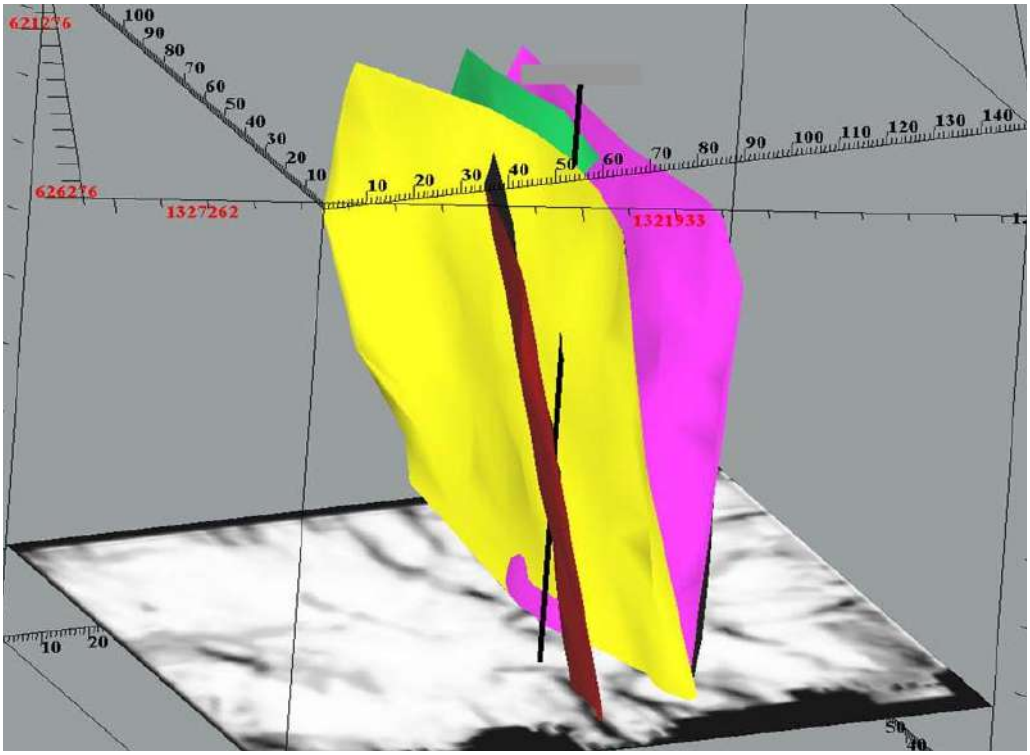

Figure 2.13. The fault planes shown with well W2. Well W2 intersects two of the fault planes – the yellow and the red.

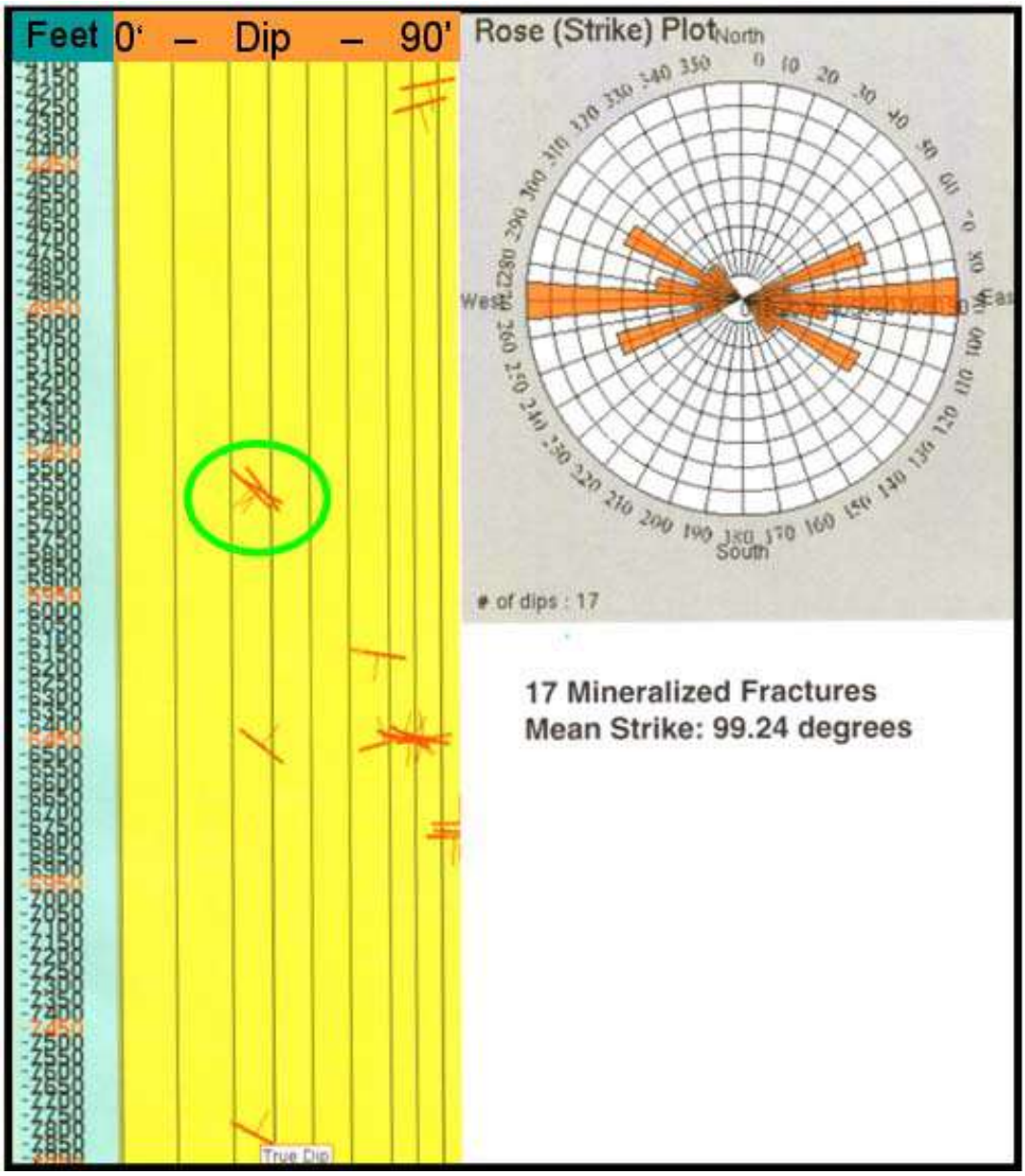

Figure 2.14. On the left side of this image is a depth log of mineralized natural fractures showing the strike, dip, and depth of each fracture. On the right side of this image is a rose diagram showing the cumulative strikes of all the mineralized fractures from the log on the left. The fractures interpreted at approximately 5600ft circled in green have a distinctly different strike and dip than the others. They strike in the same direction as the fault that cuts at approximately that depth. (Hargrow, 2006)

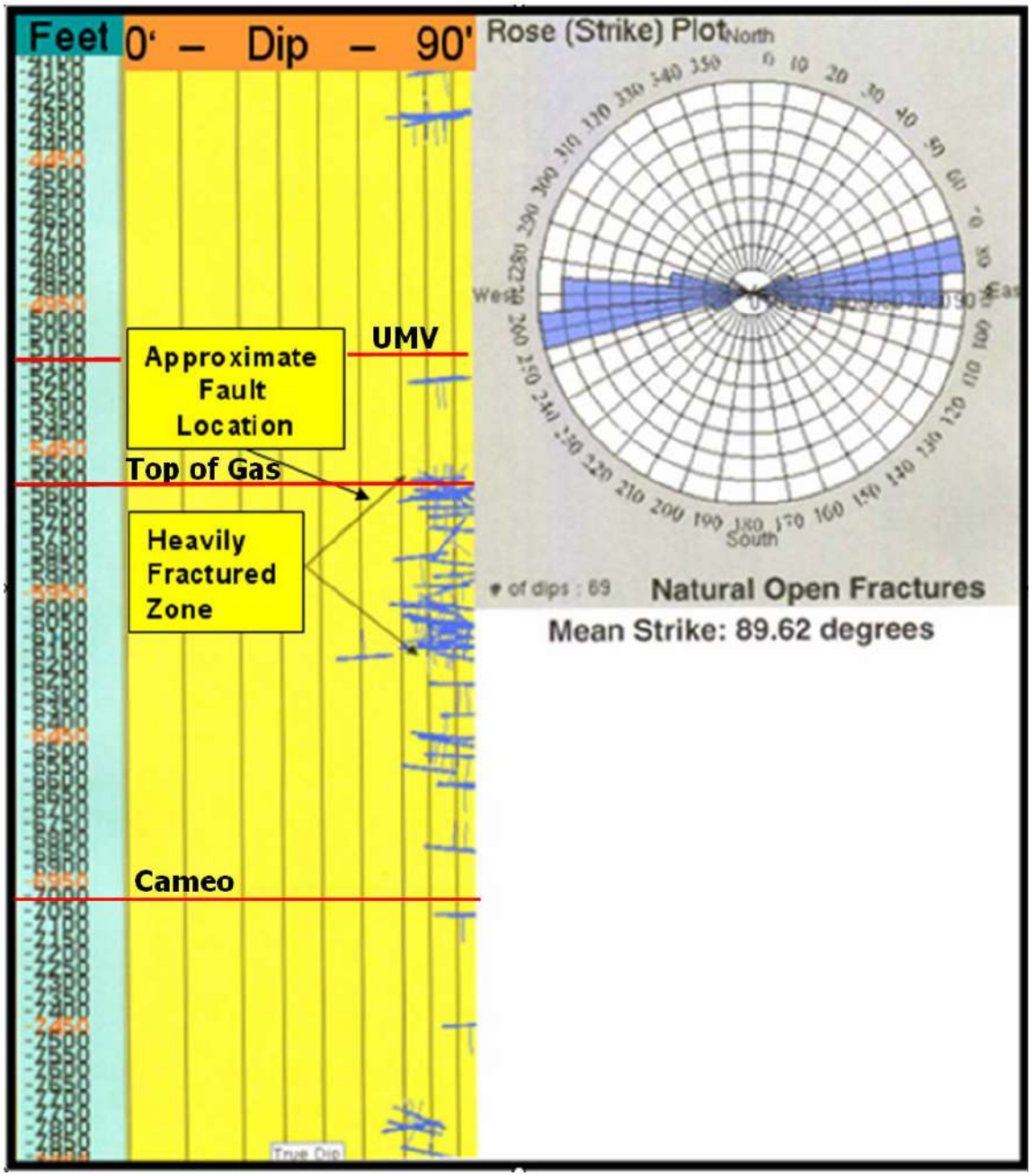

Figure 2.15 Log of the natural open fractures from well W2 showing the strike and dip of every interpreted natural fracture. On the right side of this image is a rose diagram showing the strikes of all the natural open fractures on the left. Notice how there is a heavily fractured zone near the fault location at 5600ft. (modified from Hargrow, 2006)

Since the existence of some of these faults has been confirmed, high and low EUR wells are used to explore the affects of these faults on production. The three highest EUR wells and the three lowest EUR wells in the high fold area of the survey show that the high EUR wells are near the faults or intersect them and the low EUR well significantly farther away from the faults.

The high EUR wells, H1, H2, and H3 are shown with the faults in figure 2.16. Well H1 does not intersect a fault but is only a few hundred feet to the west of the pink fault through the entire reservoir as the pink fault is nearly vertical in this area of the reservoir. This well is the best well in the field and has been producing high rates of natural gas since 1981 with less decline than surrounding wells. Well H2 crosses the yellow fault in the upper reservoir and the red fault in the lower reservoir. Well H3 cuts the yellow fault in the upper reservoir and the distance between the borehole and the fault plane increases with depth as the fault is dipping away from the borehole. All of the high EUR wells cut the faults or are within a few hundred feet of the faults.

The low EUR wells, L1, L2, and L3, are shown with the fault in map view in figure 2.17. None of the low EUR wells intersect the faults or are near the faults. Well L2 is over a thousand feet west of all the faults, and well L3 is over two thousand feet east of any of the faults.

These results indicate that there is a relationship between the EUR of a well and the distance between a wellbore and a fault. The wells with the highest EUR values are drilled near or through the faults, and the wells with the lowest EUR values are at least one thousand feet away. The high EUR wells likely produce more gas because the faults

increase natural fracture density in surrounding reservoir sandstones because of the change in stress state that the faulting causes.

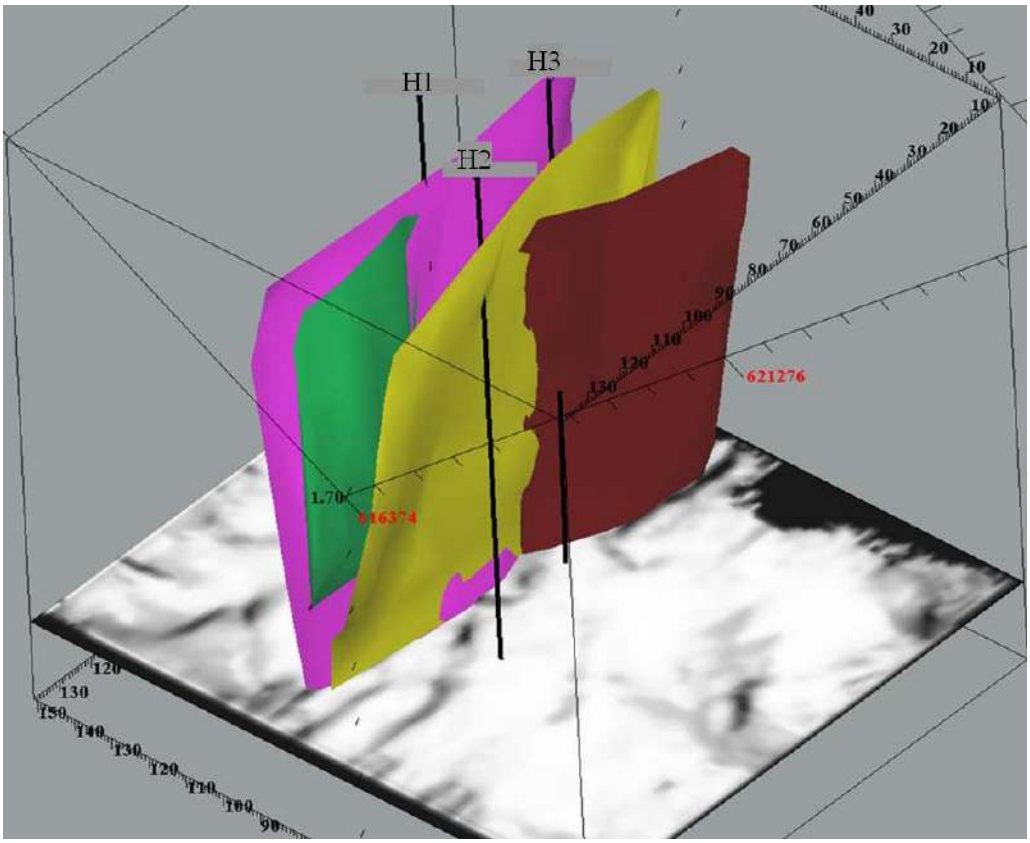

Figure 2.16 3-D view of the high EUR wells and fault planes propagating up from a depth slice of the S1 similarity volume at a depth below the Cameo horizon.

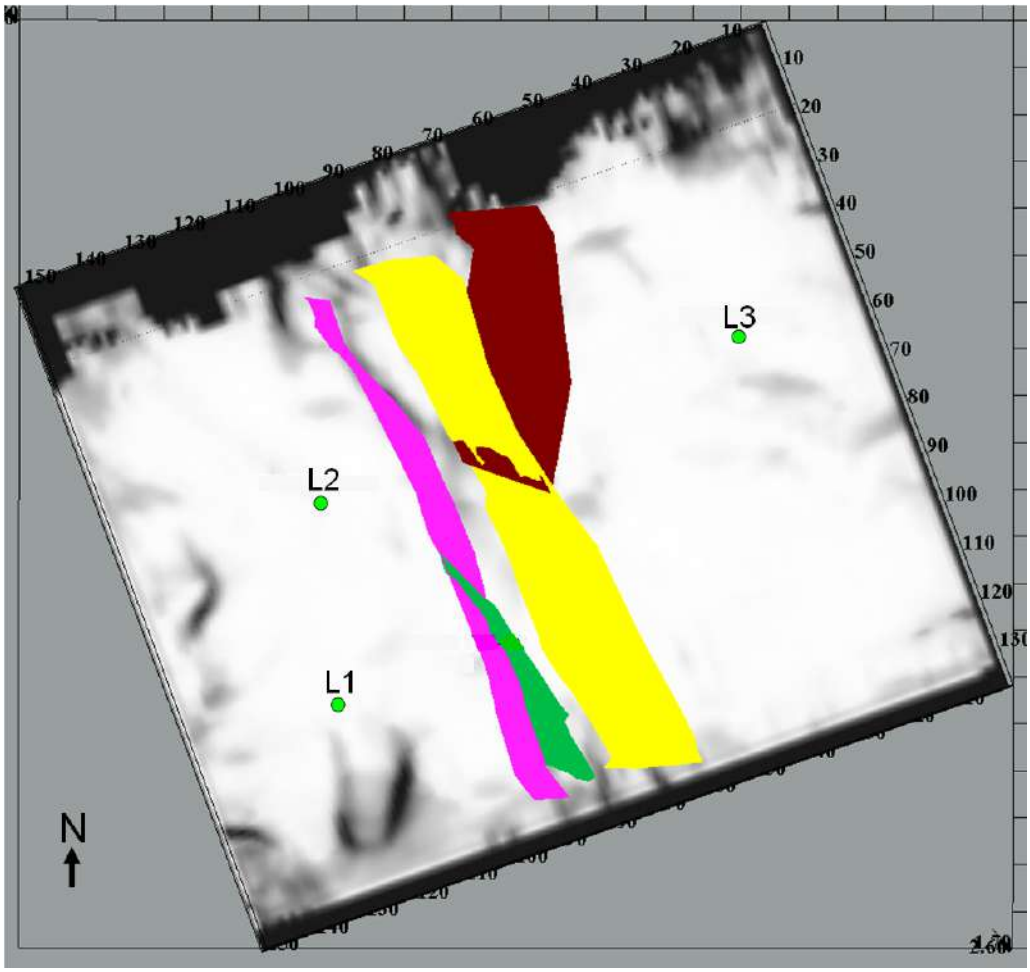

Figure 2.17 Map view of the low EUR wells and the faults planes intersecting a depth slice of the S1 similarity volume at a depth below the Cameo horizon.

2.5 Conclusions

Faults can be accurately imaged and interpreted from S-wave seismic in the reservoir interval of Rulison Field. These faults were interpreted from the S-wave data using similarity depth slices and vertical S-wave seismic displays using interpretation techniques analogous to conventional P-wave seismic interpretation techniques. Four fault planes were interpreted and formed a compressional flower structure. They are all connected at depth and diverge upwards.

Image log data from wells W1 and W2 have confirmed the locations and existence of the two of the interpreted fault planes, the yellow and pink fault planes. The

red fault plane could not be confidently confirmed by the image log, but was detected by microseismic work by Riley (2007). The location or existence of the green fault could not be confirmed since a borehole with an image log did not cut this fault.

The presence of reservoir level faulting identified with S-wave seismic in a wellbore or near a wellbore appears to increase the EUR of the well. The locations of three wells with high EURs and three wells with low EURs were compared to the locations of the faults. The three wells with high EURs either intersected the faults or were within a few hundred feet of the faults through most of the reservoir. The low EUR wells were significantly farther away from the faults. This relationship implies that wells drilled closer to the faults produce more gas. This is likely because faulting increases the density of natural fracturing and therefore the permeability of the reservoir which will allow more gas to flow to the wellbore. These faults and their surrounding fractures could also be conduits for natural gas migration from the coals. If the upper reservoir is consistently being recharged with natural gas via open natural fracture networks associated with this sort of faulting, this would explain the anomalously high and steady production of well H1. Even though this well never crosses a major fault it is within a few hundred feet of one through most of the reservoir and could cross many smaller fault splays and fracture zones that are below seismic resolution.

CHAPTER 3 S-WAVE SPLITTING ANALYSIS AND OBSERVATIONS

Image logs and core data confirm that the reservoir sandstones in Rulison Field are heavily fractured in some areas and relatively unfractured in others. The presence of dense fracturing in a wellbore has been shown to greatly increase natural gas production by increasing permeability (Lorenz and Finley, 1991). Efforts to predict changes in fracture intensity using conventional S-wave splitting techniques are complicated by the thickness and lack of consistent reflectors through much of the reservoir. Past research on fracture density from S-wave seismic by Jansen (2005) and Vasconcelos (2007) was limited by the horizon-based aspect of both of their approaches. They only estimated the fracture density in large intervals and did not tie their data to fracture density from cross-dipole and image logs through reservoir interval.

An example of natural open fracture variation with depth in Rulison Field can be seen on figure 2.15. Fracture density is high between 5570 and 6160 feet. This interval is over 400 feet below the UMV shale horizon and 900 feet above the Cameo coal horizon. S-wave splitting parameters calculated in the gross interval from the UMV shale to Cameo estimates little to no anisotropy in the gross interval. To accurately predict thin-bed variations in fracture density in Rulison Field, a new approach is necessary.

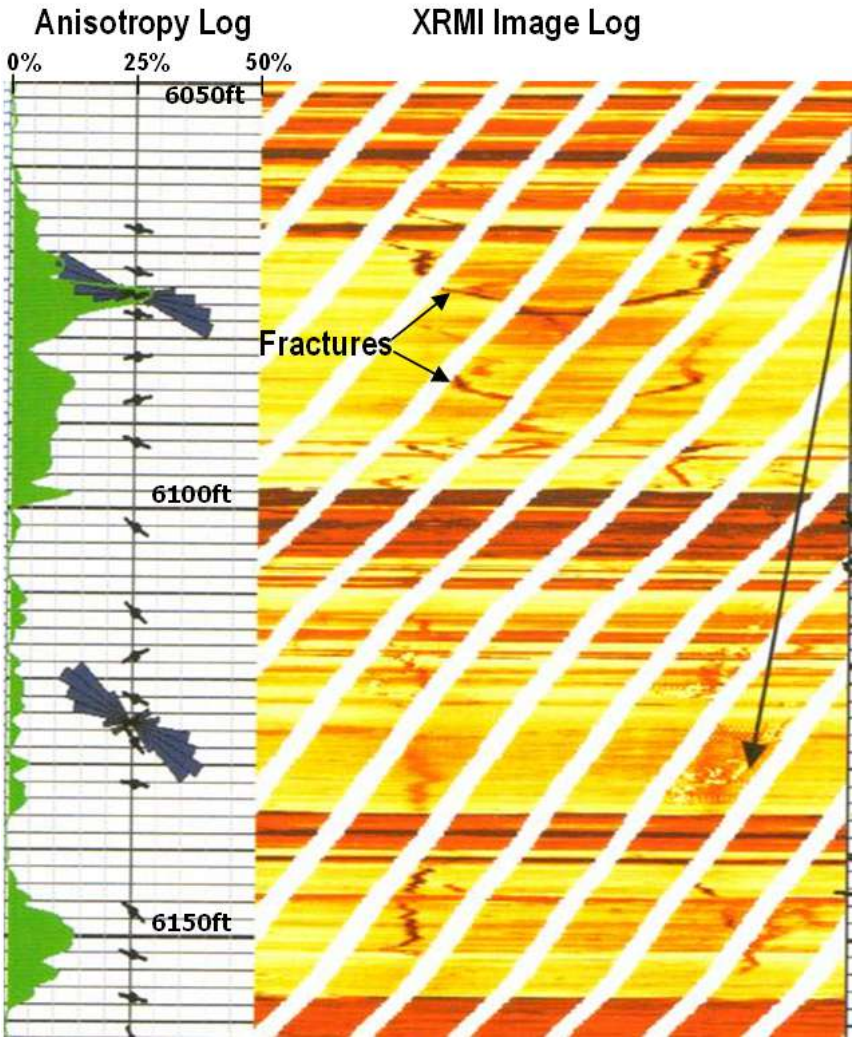

Figure 3.1 Anisotropy and XRMI image log from well W1 showing the correlation between fractures imaged by the XRMI image log and anisotropy calculated from S-wave splitting recorded by cross-dipole sonic log.

A hundred foot middle reservoir section of the XRMI image log and anisotropy log from the cross-dipole sonic tool is shown in figure 3.1. The image log shows sandstones in yellow and shales in orange to brown. Fractures are shaded in the sandstones in orange or brown. The anisotropy log shows high anisotropy in the densest fractured sandstones and nearly zero anisotropy in the shales. The anisotropy log is calculated from S-wave splitting, or S1 and S2 velocity differences. In this chapter, I evaluate the link of S-wave splitting from surface seismic to subsurface fracture density

and show that S-wave splitting can estimate fracture density and resolve the fractured reservoir sandstone intervals.

3.1 Methodology

Conventional methods of estimating azimuthal anisotropy from S-wave splitting are horizon based algorithms that use travel-time differences between the S1 and S2 components (Martin and Davis, 1987 & Thomsen, 1988). Jansen (2005) presents the results of these methods at Rulison Field using the RCP S-wave seismic, and the downfalls of these methods are discussed in the previous section. My methods of calculating S-wave splitting is based on the theories of travel-time, amplitude, and attribute difference developed by Martin and Davis (1987) and Thomsen (1988), respectively, but employs a volumetric multi-step approach that has never been used before. This method uses no interpreted horizons and is applicable to thick reservoirs without continuous reflectors that can be confidently picked on both volumes. The other major difference between this method and past methods is they estimate S-wave splitting parameters from amplitude volumes, and my method explores S-wave splitting parameters of S1 and S2 “coloured” inversion volumes and S1 and S2 similarity volumes. The coloured inversion maps the mean seismic amplitude spectrum to the mean impedance spectrum of the earth with a 90 degree phase shift (Lancaster and Whitcombe, 2000). Michael Rumon (2006) created the coloured inversion volumes. He created these volumes with Hampson-Russell’s colored inversion software. The inputs for this inversion program are seismic amplitude data and S-wave well log data. Rumon used the 2003 S1 and S2 seismic volumes and the S1 and S2 S-wave logs from a well in the southeast part of the field. Therefore, the impedance volumes that result from coloured

inversion are phase shifted and impedance-value scaled volumes that retain the frequency and overall seismic character of the original amplitude volumes.

The first step of this method is to calculate the travel-time differences between the S1 and the S2 volume. This was done using the registration algorithm in Transform Software's TerraMorph™ package. This program uses a registration algorithm similar to the algorithm presented by Fomel et al. (2005) and was originally developed to shift converted-wave seismic into the P-wave seismic time domain. This algorithm uses a window-based, cross-correlation, time-variant, time-shifting approach to calculate the difference in travel-time between the S1 and S2 volumes at every sample by matching corresponding reflections in the S2 volume to the S1 volume. This algorithm shifts the S2 data into the S1 time domain. A sample seismic line showing the differences between the original S2 data and the shifted data is shown in figure 3.2. This algorithm required four user inputs. The first is to select the range of two-way travel-times of each volume to match. I used 1500 to 3000 milliseconds; this range covered the reservoir and a large buffer zone above and below the reservoir. The second input is the amount of travel-time to bulk shift the S2 data to approximately match the S1. I subtracted 30 milliseconds of travel-time from the S2 dataset. The third user input is the window length that algorithm is allowed to search for a match for any given sample after it has adjusted the volume to the time shift of the overlying sample. I used 30 milliseconds for this parameter. The final user input is the distance surrounding the trace that is used to help find the proper reflector match. This is necessary because impedance values from the inversion volumes vary significantly through the survey and the values of the two components should not be the same. I used 550 feet for this parameter. I decided on these parameters by using a trial

and error method. An output volume of this process is a correlation coefficient volume. The values listed above created the most consistent high correlation coefficient volume.

At the end of this step, three new seismic volumes have been created. The first of these is the correlation coefficient volume discussed above. The second volume is a direct measurement of velocity anisotropy that provides a low resolution estimate of the cumulative anisotropy through the reservoir. Figure 3.3 shows a 3-D cube of this volume. The travel-time differences, and therefore, the S1 and S2 velocities change rapidly both spatially and vertically. These differences in the amount of travel-time are a cumulative measure, and the difference at any given depth is the result of the cumulative differences above.

The third volume created by this step is a warped version of the original S2 volume. This volume contains the impedance values of the S2 volume but has been stretched and squeezed on the time axis to shift the values into the S1 time domain. Data in the areas where reflectors could not be matched properly were not used for the analysis and interpretation. To correct the majority of the dataset for this problem, the low fold portions of the survey were trimmed from these volumes and all subsequent volumes. The low fold area that was trimmed are the 20 lines on the east and west edges of the inline direction, and the 40 lines on the north edge and 30 lines on the south edge of crossline direction. Figure 1.13 shows the original survey with the trimmed areas shaded gray. Figure 3.4 shows the high fold area of a crossline through the center of the survey with the S1 and warped S2 volume display together using a corendering technique. The S1 volume has a red to white scale, and the warped S2 volume has a blue to white scale. Where the volumes match, a gray scale is created by the red and blue scale interference;

where they don't match blue and red can be seen due to the lack of color interference. These volumes are very well matched at the high impedance reflectors but are not perfectly matched in the low reflectivity zones.

The next step of my S-wave splitting method is to calculate the difference between S1 and warped S2 impedance inversion volumes. This is a well that is not in my trimmed area of the survey so I did not use this well for any of my comparisons. The final inversion volumes have elastic impedance values. Elastic impedance is equal to density multiplied by S-wave velocity, and the units of these volumes are (feet*grams)/(milliseconds*cubic centimeter) which results in all large positive values. Rumon provides a detailed workflow of how he created these volumes in his thesis.

The mathematical formula used to calculate the volumetric difference between the elastic impedance volumes is shown below.

Equation 3.1

$$IA = \left| \frac{S1 - S2}{S1} \right| = \left| 1 - \frac{S2}{S1} \right|$$

In this equation, IA is impedance anisotropy, S1 is S1 elastic impedance volume, and S2 is warped S2 impedance volume. Since the values in the impedance volumes are all large positive values, this equation essentially calculates the percent difference between the two impedance volumes. Approximate value range for this volume is 0% to 10% with most values near zero. This volume is a higher resolution anisotropy calculation than the travel-time difference volume and will be discussed in detail in the next section.

The final step of my method of S-wave splitting is to volumetrically difference S1 and warped S2 similarity volumes. This sort of seismic attribute S-wave splitting evaluation allows waveform changes in the S1 and S2 to be compared. The same

similarity volumes created for the fault interpretation portion of this research were used for this S-wave splitting calculation. There are two inputs for this algorithm: time window length and number of surrounding traces to compare to. I used a window length of sixty-four milliseconds and eight surrounding traces. The S2 similarity volume was warped into S1 time by applying the travel-time differences calculated by warping the amplitude data to the similarity data instead of using the registration software to match the S1 and S2 similarity volumes. This is because the lack of repeatable frequency in this type of volume makes the travel-time differences calculated by the algorithm unreliable.

The formula used for calculating the sample by sample difference in the S1 and warped S2 similarity volumes is shown below.

Equation 3.2

$$SD = S1_{SIM} - S2_{SIM}$$

In this equation SD is the calculated similarity difference volume, $S1_{SIM}$ is the S1 similarity volume, and $S2_{SIM}$ is the warped S2 similarity volume. The values in the similarity volumes range from 1 to 0%. A value of 1 is defined as the evaluated windowed section of a trace being completely the same as the surrounding traces, and a value of 0 is defined as the evaluated windowed section of a trace is very dissimilar from the surrounding traces. Most of the values in these volumes are above .80 indicating that nowhere in the volume in is one trace completely different from the traces surrounding it. Therefore, the equation above evaluates the difference between the similarity volumes, and the differences will always be between 1 and -1. Values generally fall between .30 to -.30 with most values near zero. This volume will be interpreted and discussed in detail in section 3.3.

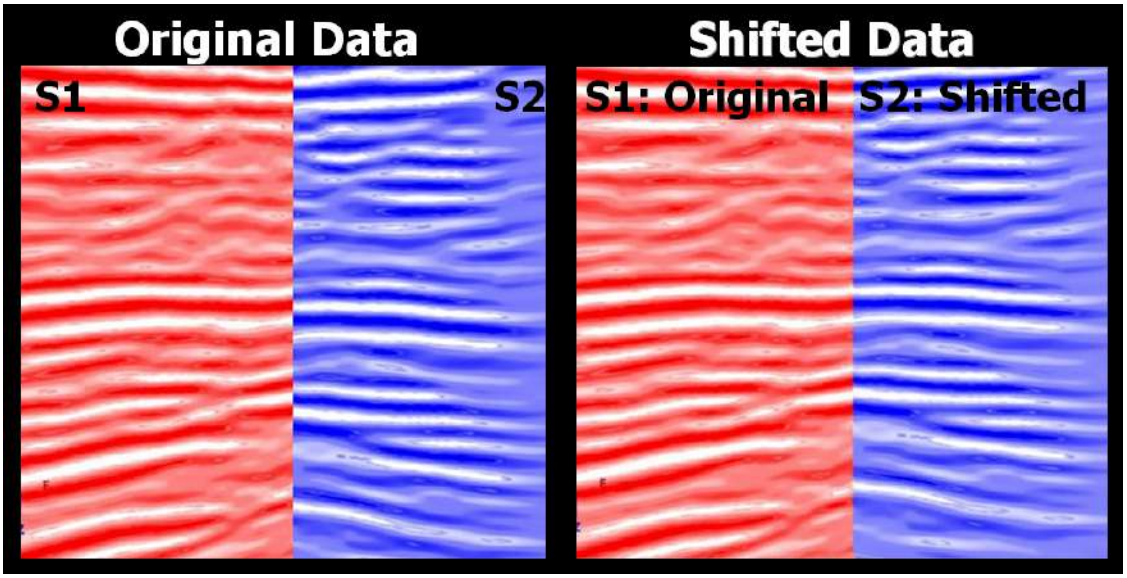

Figure 3.2. On left, original S1 & S2 volumes. On right, original S1 volume & time shifted S2

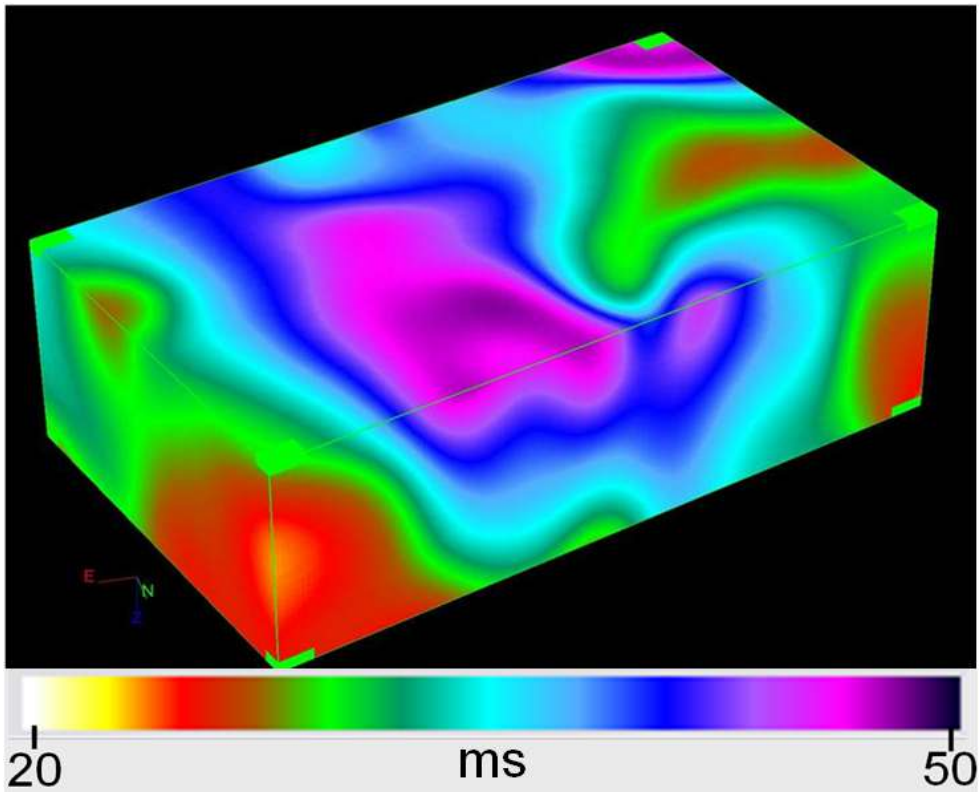

Figure 3.3. A 3-D prism showing the travel-time difference volume.

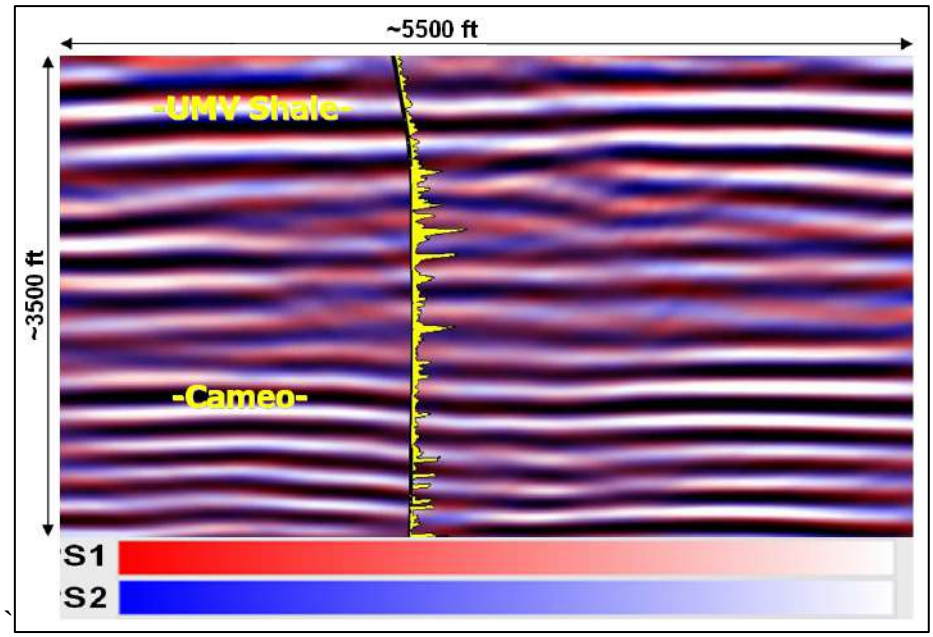

Figure 3.4. Crossline 71 of the fast and slow time-shifted volumes correndered with the anisotropy log from well W1 overlain in yellow.

3.2 Impedance Anisotropy

Impedance anisotropy is a high resolution tool for measuring azimuthal anisotropy and is the approximate percent difference between the S1 and warped S2 elastic impedance inversion volumes. Thomsen (1988) stated that amplitude anisotropy is a much higher resolution tool than time anisotropy because one is a local measure and the other is an integral measure. Since impedance anisotropy is also an integral measure and impedance inversion increases seismic resolution, impedance anisotropy should be a higher resolution tool than amplitude anisotropy.

Figure 3.5 shows crossline 54 through the impedance anisotropy volume. The scale bar for this image goes from 0% to 7%. 0% to 2% is colored gray because these values are below the resolution and within the expected error of the volume. The areas above 3% impedance anisotropy and above are caused by significant differences between the S1 and S2 impedance values that are caused by S-wave splitting. These groups of high impedance anisotropy are rarely more than 500 feet wide and 500 feet thick in the

high fold area of the reservoir. Some wellbores intersect parts of these groups, but many do not. Areas along the edges of this volume have anomalies larger than 500ft thick or wide, but this is because the traveltime difference calculated by the registration algorithm poorly matched some of the low fold area due to frequency cycle skips. The correlation coefficient volume shows a lower correlation in these areas. The edges of the volume where excessively large anomalies exist are unreliable. The most reliable areas in the volume are where the fold is over 100. This volume has a frequency component that can be seen in figure 3.5. This is an artifact of the frequency component of the impedance volumes.

These volumes should correlate with seismic scale changes in azimuthal anisotropy measured by cross-dipole sonic logs. To confirm this statement, I compared the anisotropy log from well W1 with the traces in the impedance anisotropy volume near the borehole. Figure 3.6 shows the smoothed anisotropy log from well W1 and inline 86 which intersects well W1. The anisotropy log has been smoothed by a centered 50 ft moving average to lower the resolution to a value similar to that of the seismic. Both the log and the seismic are shaded with the same color bar. Since the seismic fold at this borehole is over 200, the impedance anisotropy volume should be accurate at this location.

The anisotropy values of the seismic at the wellbore and the log are remarkably consistent. A true correlation coefficient between the seismic at the wellbore and the log cannot be calculated due to the frequency component of the impedance anisotropy volume, but a qualitative zone by zone comparison can be done. From the top of the log to 1.9 s in depth, both the seismic and log detect anisotropy values less than 2%. Between

1.9 s and 2.1 s, the impedance anisotropy volume is detecting anisotropy values over 3% and the log has many anisotropy values over 3%. Between 2.1 s and 2.25 s, the anisotropy volume has values consistently below 2% and the log has values below 2% with the exception of one 15 ms spike of anisotropy log values up to 7% at 2.18s. Between 2.25 s and 2.32 s, the seismic and log anisotropy values range from 0% to 4%. Below this and before 2.44 s, both the log and seismic anisotropy values are below the 2% resolution threshold. From 2.44 s to 2.54 s, the log and the seismic show similar variations between 0% and over 5% anisotropy. The log and seismic below this point both read values below 2%. The only poor correlation between the anisotropy log and seismic is at the spike at 2.18 s. This could be caused by a small scale localized fracturing that is spatially and vertically below the seismic resolution. The rest of the seismic and log anisotropy values are consistent with either other. The positive correlation between the log and seismic anisotropy values confirms that the impedance anisotropy volume is accurately detecting seismic scale changes of the azimuthal anisotropy of the reservoir rock. The image log of this well which was interpreted by Matesic (2007), shows that the anisotropy log values increase through areas of increased natural fracturing. Therefore, the impedance anisotropy volume is detecting changes in natural fracture density.

If the impedance anisotropy volume can detect seismic scale fracture swarms, this volume should be able to predict the locations of the best and worst wells in the field based on whether the borehole cross areas of high impedance anisotropy. To test this theory, I compared the high and low EUR wells to the impedance anisotropy traces surrounding the borehole. Figure 3.7 shows a crossline through the impedance anisotropy volume that intersects well H1 shown as a black vertical line. The impedance anisotropy

values near this well are over the 2% threshold limit through most of the area between the UMV and Cameo horizon, and then stay below 2% below the Cameo horizon. Based on these numbers well W1 is connected to many fracture networks between the top of the Cameo and UMV shale. This same conclusion was reached about this well in the faulting section. This well is drilled a few hundred feet from one of the interpreted strike-slip faults. This fault is the pink line in figure 3.7. Because of its proximity to the fault, the conclusion was made in chapter 2 that that this well connected to many of the fracture swarms associated with the fault through the entire interval. The impedance anisotropy volume confirms this conclusion and that there is an increase fracture density near this fault.

Figure 3.8 shows well H2 overlain on the impedance anisotropy volume. This well has one of the highest EUR‘s in the field and crosses an area of very high impedance anisotropy in the upper reservoir and below the Cameo horizon. The faults that this well cuts are displayed in yellow and red. The area of high impedance anisotropy and therefore denser fracturing is located just above the yellow fault, but not between the two faults or below the red fault. This suggests that while faulting tends to be associated with natural fracture density, natural fracture density is not increased equally around the fault. Open natural fracturing can be limited to certain areas of the fault that are likely caused by stress.

Figure 3.9 shows low EUR well L2 at the location that it intersects the impedance anisotropy volume. Most of the low EUR wells are located in areas of the survey with less than 100 fold. Of the low EUR wells, this well is located in the area of highest fold. The impedance volume is not as dependable at this location, but this well is still worth

comparing with the impedance anisotropy volume to see if this volume can be used to predict the location of low EUR wells.

This well only crosses one area of high impedance anisotropy located in the upper reservoir. Therefore, the well should encounter fracturing in the upper reservoir and lack of fracturing is likely not the reason for the poor EUR of this well. The problem predicting wells with poor production is that there are some many other factors that could lower the production of the well.

In conclusion, impedance anisotropy is a new way to estimate S-wave splitting parameters by volumetrically calculating the differences between S1 and S2 elastic impedance inversion volumes. The tie between the high and low areas of the impedance anisotropy volume and the W1 anisotropy log shown in figure 3.6 suggests that this volume is vertically as well as laterally estimating S-wave splitting parameters related to fracture density.

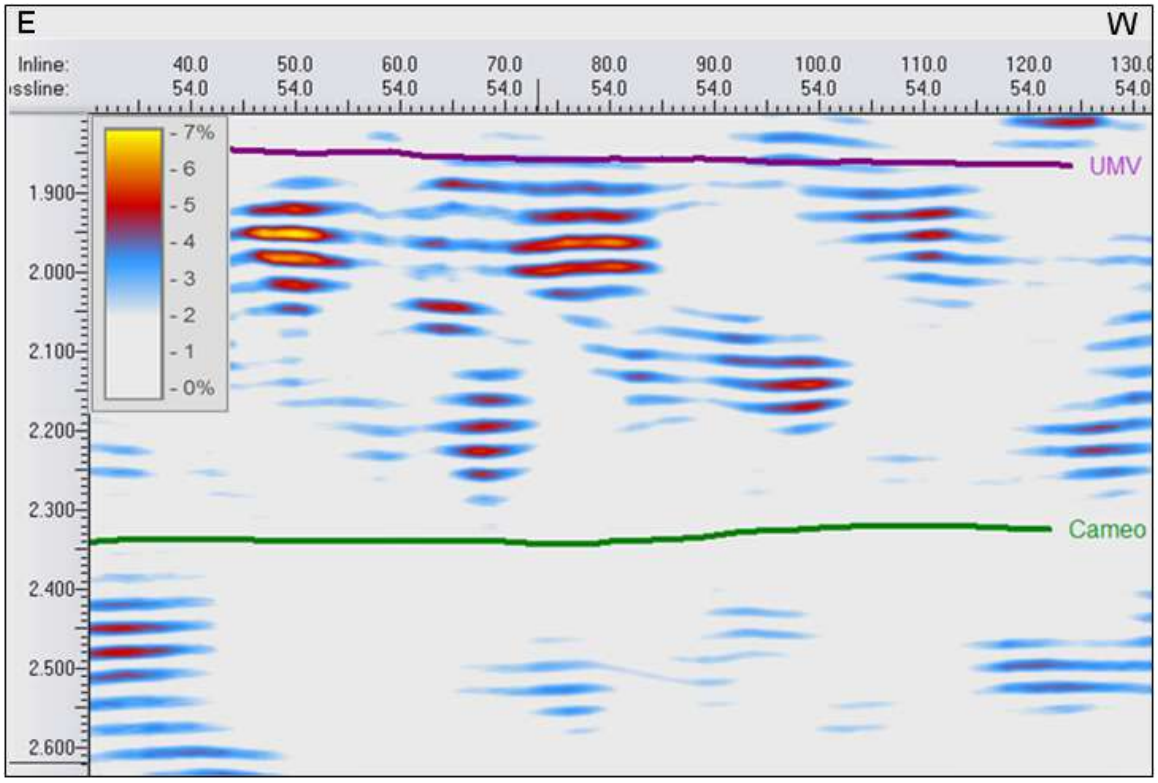

Figure 3.5 Crossline 54 through the impedance anisotropy volume

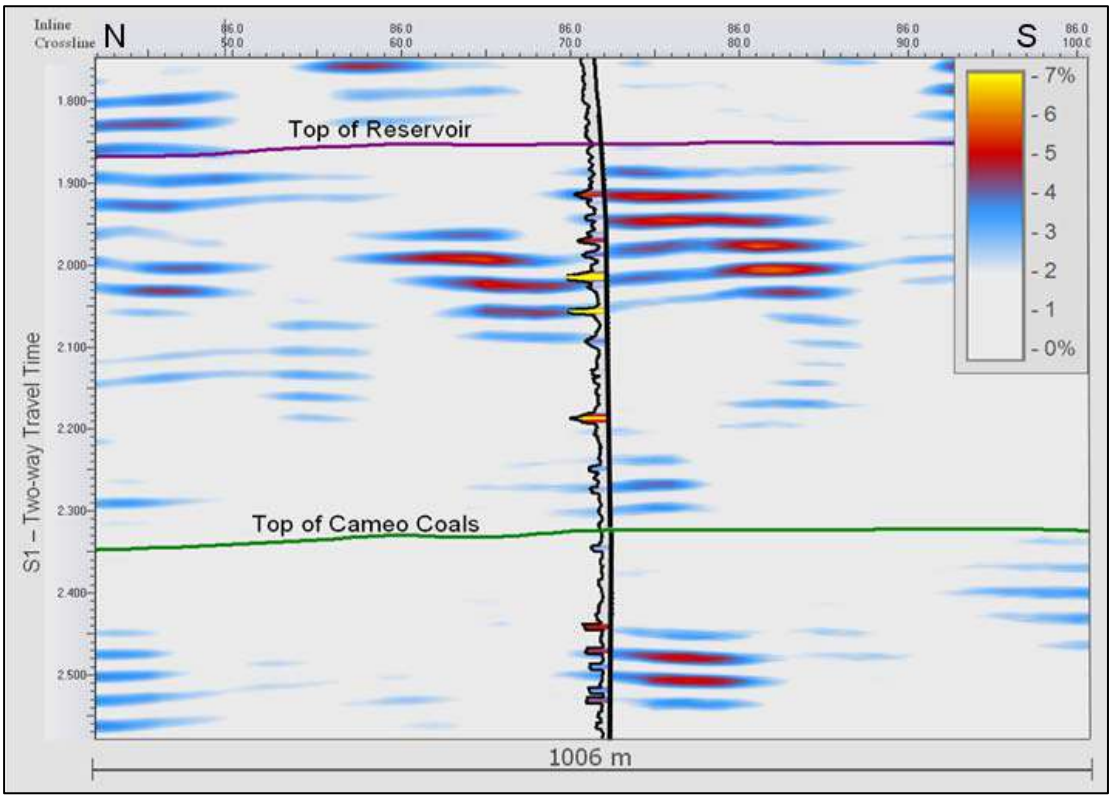

Figure 3.6 Inline 86 from the impedance anisotropy volume with the anisotropy log from well W1 overlain and shaded with the same colorbar.

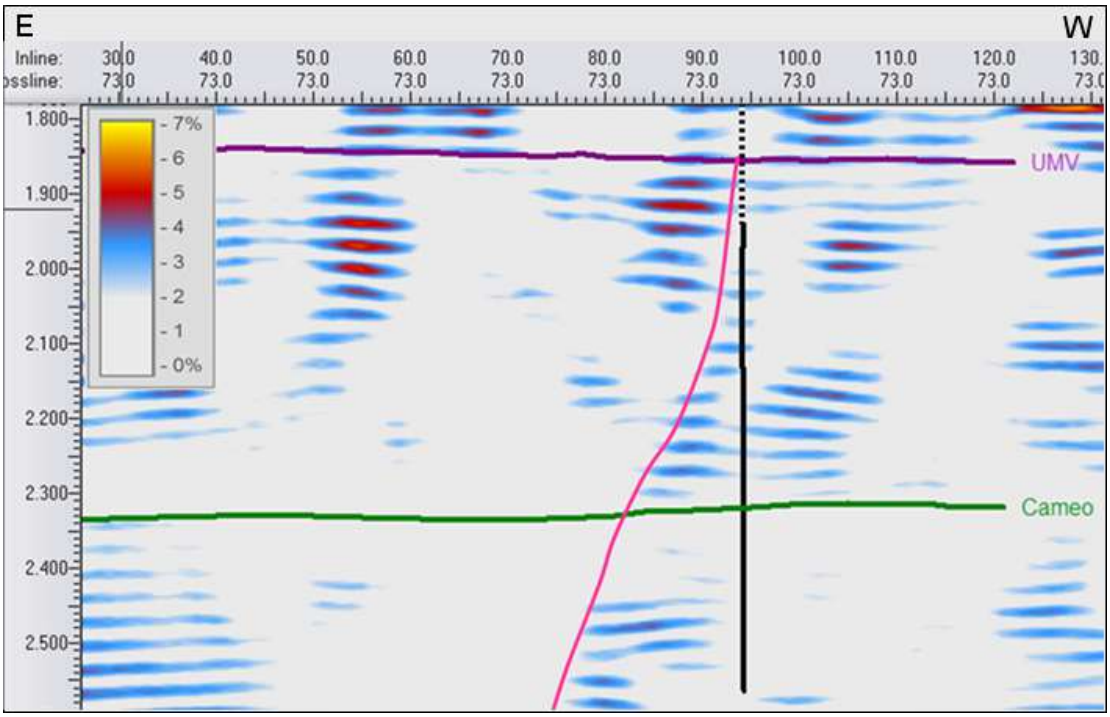

Figure 3.7 Crossline 73 through the impedance anisotropy volume with well H1 overlain in black.

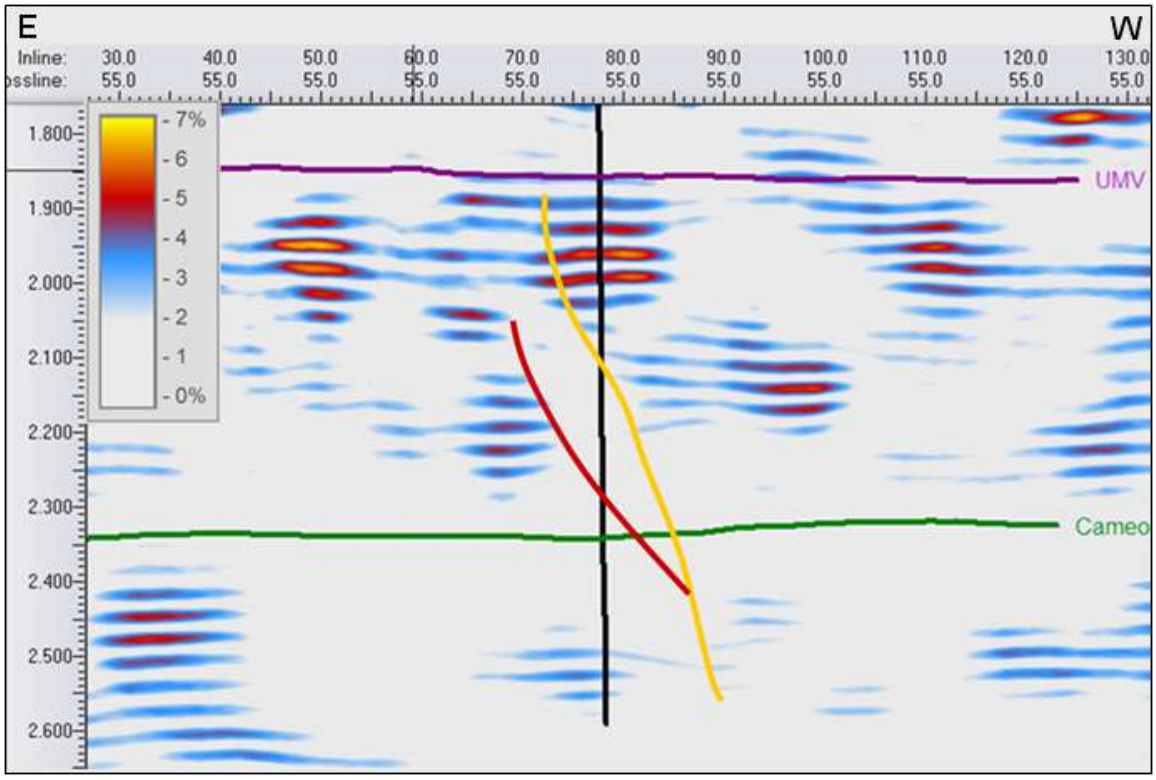

Figure 3.8 Crossline 55 through the impedance anisotropy volume with at the location of high EUR well H2.

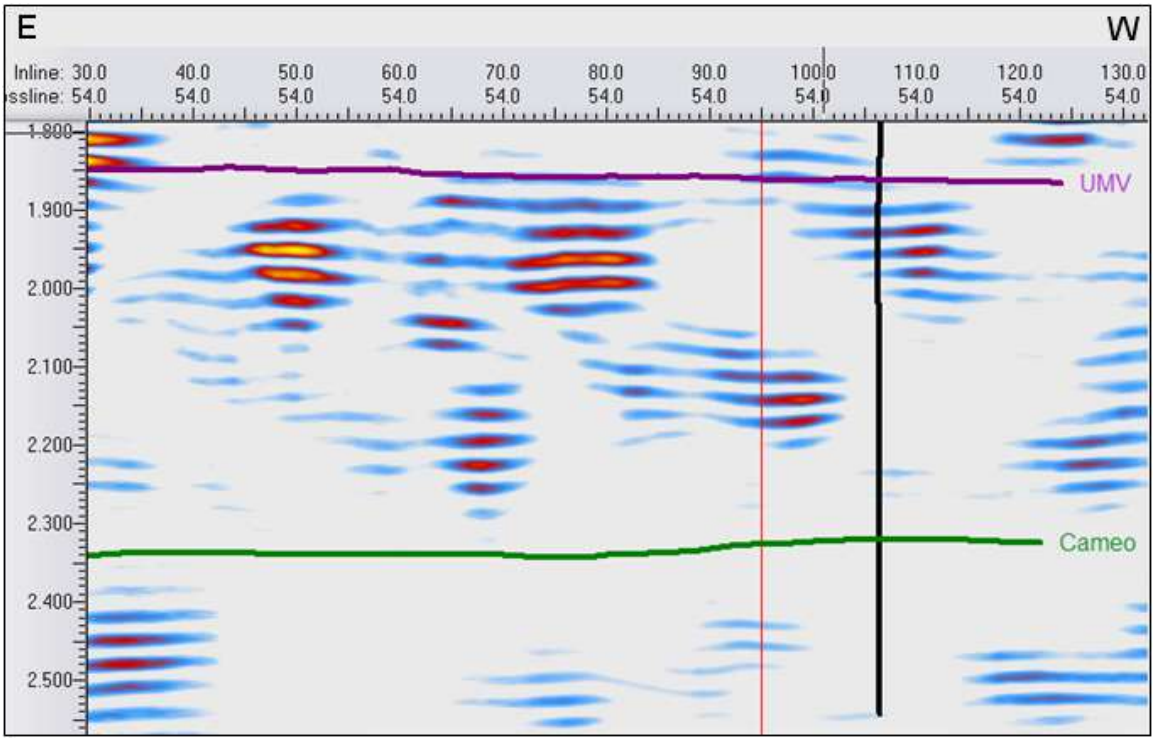

Figure 3.9 Inline 54 through the impedance anisotropy volume with intersecting low EUR well L2 overlain in black. The colorbar for this figure is the same as the colorbar for the pervious figure.

3.3 Similarity Difference

Similarity is a coherency-like attribute that is conventionally used to help with structural interpretation because it detects changes between traces. In layered, relatively flat bedded rock, it will detect faults that displace the rock more than the seismically resolvable distances because the seismic reflection shifts causing a change in amplitude or apparent frequency at the location of the fault. In fluvial environments, seismic rarely detects a consistent reflector so similarity detects the edges of these inconsistent reflectors that may or may not be structurally related. If, in fluvial environments, similarity detects an edge that creates a surface through the seismic, this is likely a fault. These types of faults were interpreted in the Rulison Field multicomponent similarity

seismic volumes and were discussed in chapter 2. At Rulison field, similarity volumes calculated from the S1 and S2 seismic volumes can detect edges of reflectors that are not related to faulting or structure and that have small vertical and lateral dimensions. Some of these resemble the edges of fluvial channels, point bars and other stratigraphic structures seen in fluvial environments.

Figure 3.10 shows a time slice of the S1 similarity volume through the middle of the fluvial reservoir. A value of one on the similarity scale means that an edge or a difference between traces was not detected. Similarity values progressively less than one denote greater differences between traces. This figure shows many dissimilar events surrounded by similar areas. Two of these dissimilar events resemble the type of fluvial channels that occur at the edges of point bars in meandering streams. They are highlighted with black lines. The existing wells in the field as of 2006 are shown as black dots and not a single well intersects either of these possible stratigraphic features. The well highlighted in blue is very close to the possible channel. This well has an approximately fifty-foot thick sand at this depth that fines upward like a point bar sandstone. This observation supports the theory that the S1 volume is detecting stratigraphic features. In this case, the S1 volume detected the edge between a sandstone point bar and a fluvial channel. The channel is likely filled with silt or shale creating an impedance contrast detectable by seismic between the shale filled channel and fractured sandstone point bar.

The S1 and the S2 similarity volumes detect different events at the same depth. Some of the events are seen by both the S1 and the S2 volumes. Most of the events detected by both volumes are structurally related, and most of the stratigraphic looking

features are detected by only one of the similarity volumes. Figure 3.11 shows time slices through the S1 and the warped S2 volume. It is difficult to visually tell exactly which events are detected by both volumes or only one. Therefore, calculating the approximate percent difference between the volumes by using the equation 3.2 defined in the methodology section of this chapter solves this problem and creates a similarity difference volume. A time slice at the same time as the maps in figure 3.11 of the similarity difference volume is shown in figure 3.12. The events that only the S1 similarity volume detected are now magnified and given positive percent difference values. The events that only the S2 similarity volume detected are also magnified and given negative percent difference values. This volume appears to have magnified the stratigraphic channel and point bar type edges detected by the both the S1 and S2 similarity volumes and to have diminished most of the structural planar events that occurred in both volumes.

The S1 or S2 similarity volumes detect different events because the image logs show that the naturally fractured fluvial sandstones are azimuthally anisotropic. These fractured sandbodies will be imaged by one component and not the other depending on the dominate strike of the aligned near vertical natural fractures. Since this data set is rotated to N43W, the S1 component will detect fractured sandstones with an aligned dominate natural fracture strike to the southwest and the S2 component will detect sandstones with an aligned dominate natural fracture strike to the northwest.

The similarity attribute is an edge detector so it will detect the edges of these fractured sandstones where there is an abrupt seismically resolvable stratigraphic change from a fractured sandstone to an unfractured rock such as a shale. A change like this is

likely to occur between a fractured point bar and a shale filled channel. This type of relationship can be seen in figure 3.13. In this figure, the positive similarity difference values create a curve that looks like a meander in a fluvial channel. If this were a fluvial channel, there would be a sandy point bar on the inside of the channel bend surrounded by a shale filled channel. The positive similarity difference values at the edge between the channel and the point bar indicate that the point bar is fractured with a dominant strike to the west-southwest because the S1 component is detecting this event. This interpreted point bar is about 550 feet wide which is within the typical range of point bar dimensions in the Piceance Basin as defined by Cole and Cumella (2005). Figure 3.15 is from Cole and Cumella (2005) and shows the typical fluvial stratigraphy seen in the Lower Williams Fork Formation. The meander belts shown in this figure resemble the edges that are detected by the similarity difference volume.

Figure 3.14 shows a deeper time slice through the reservoir where more edges of fractured sandstones can be interpreted with all wells as of 2006 displayed and the eight test wells labeled. Most of the fractured sandstones whose edges are defined by features with high similarity difference values are not penetrated by wellbores. This suggests that high quality reservoir rock is not being adequately drained by 10-acre drilling and that to properly drain this reservoir the drill bit must be guided by the geology that can only be predicted by this sort of geophysical imaging.

The high EUR wells confirm the conclusion that the similarity difference volume is imaging the edges of fractured sandstones that are high quality reservoir rock. Figure 3.17 and 3.18 show vertical sections of this volume at wells H1 and H3. Both of these wells and well H2 intersect zones in the similarity difference volume with high positive

similarity difference values indicating that they are connected to large fractured point bar reservoirs. An observation to note from all three of these wells is that they intersect positive similarity difference values which mean that the fractured rock is dominantly fractured with a strike to the west-southwest. Since most fractures interpreted from core and image logs have west-northwest trends, this could mean that the rock has two fracture sets and the west-southwest set is dominate. Dual fracture sets would increase the fracture connectivity and allow the borehole to drain a larger area or recharge the reservoir if connected to the coals. This would account for the anomalously high production of these wells.

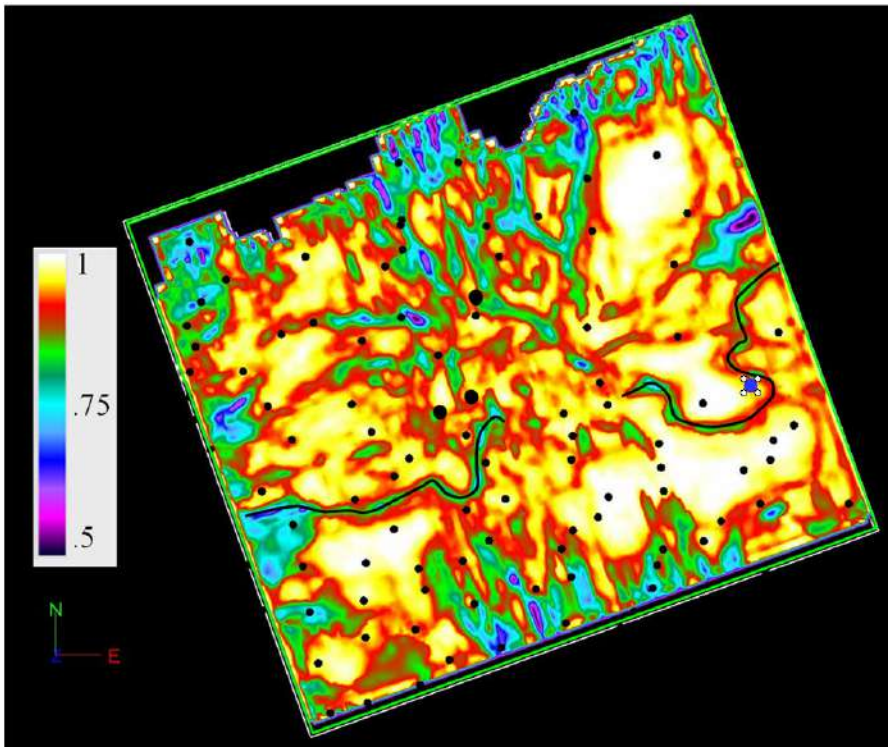

Figure 3.10 Time slice through of the S1 similarity volume through the middle reservoir fluvial environment.

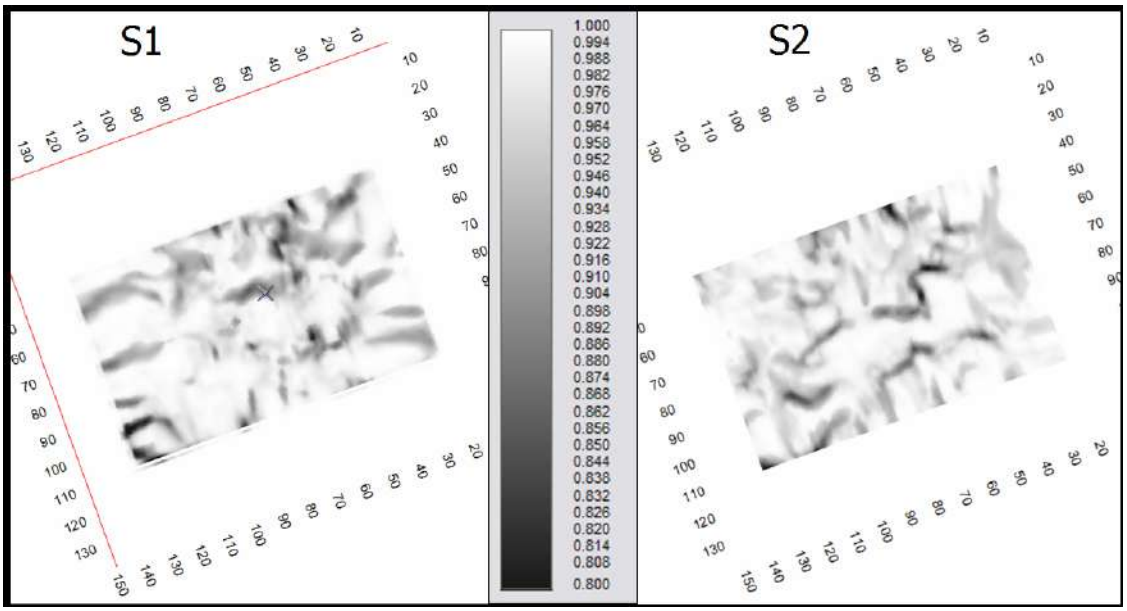

Figure 3.11 Time slices of the S1 and S2 similarity volumes through the middle of the reservoir at 1.956 seconds.

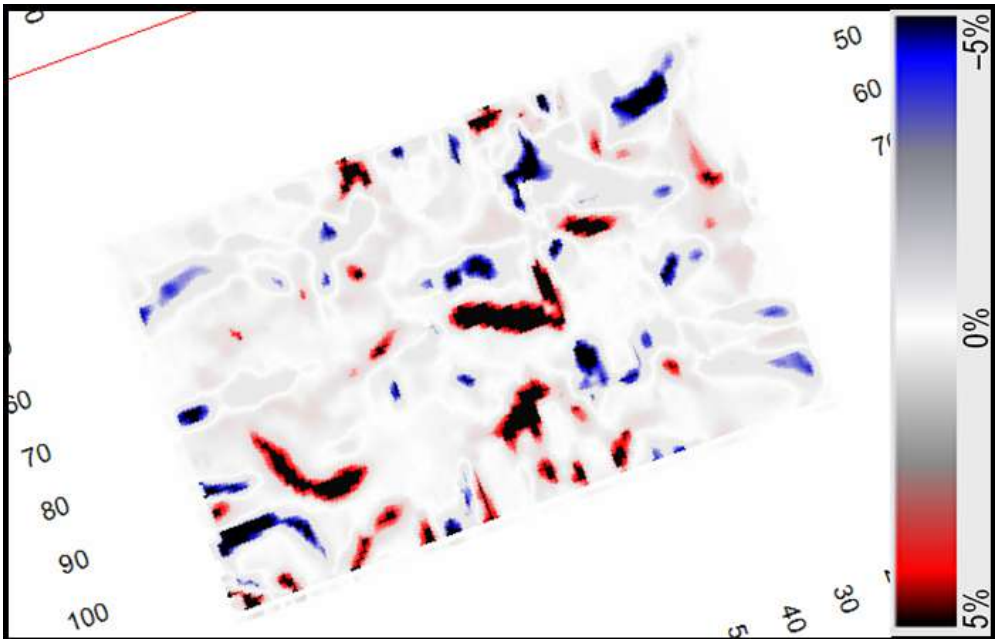

Figure 3.12 Time slice of the similarity difference volume at 1.956 seconds, same time as the slices in figure 3.11.

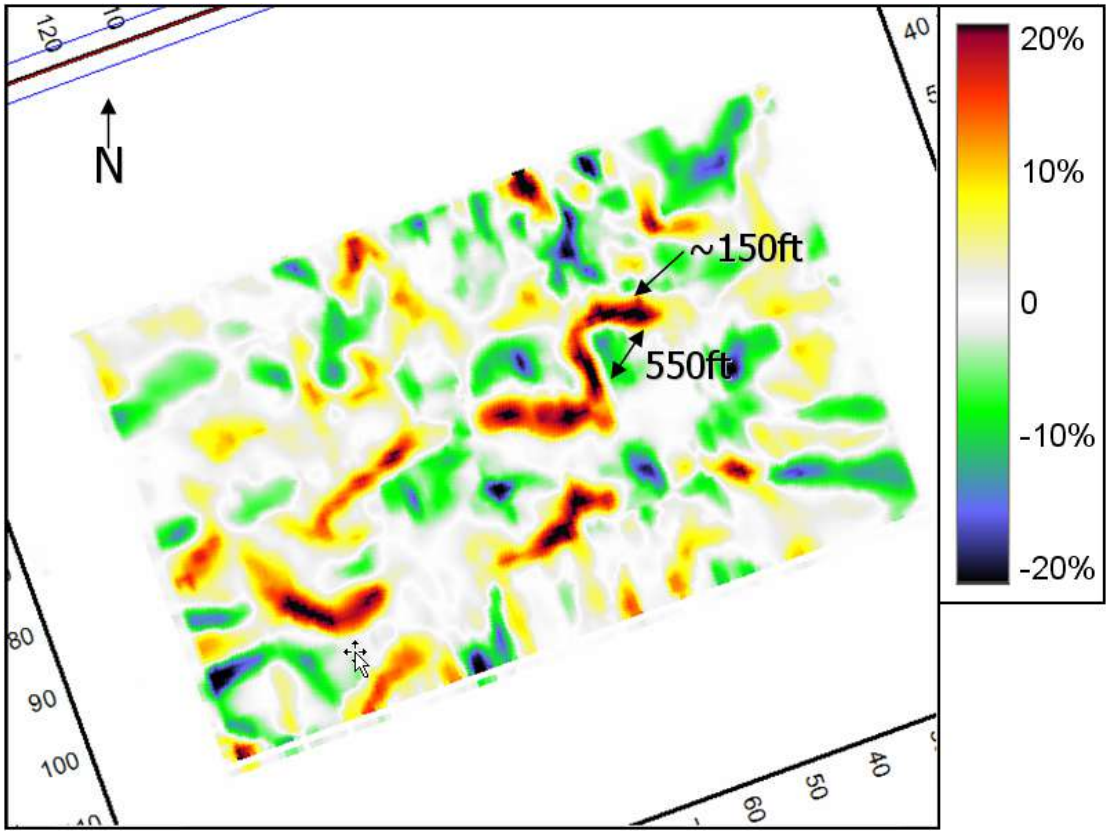

Figure 3.13 Time slice through the similarity difference volume at 1.998 seconds.

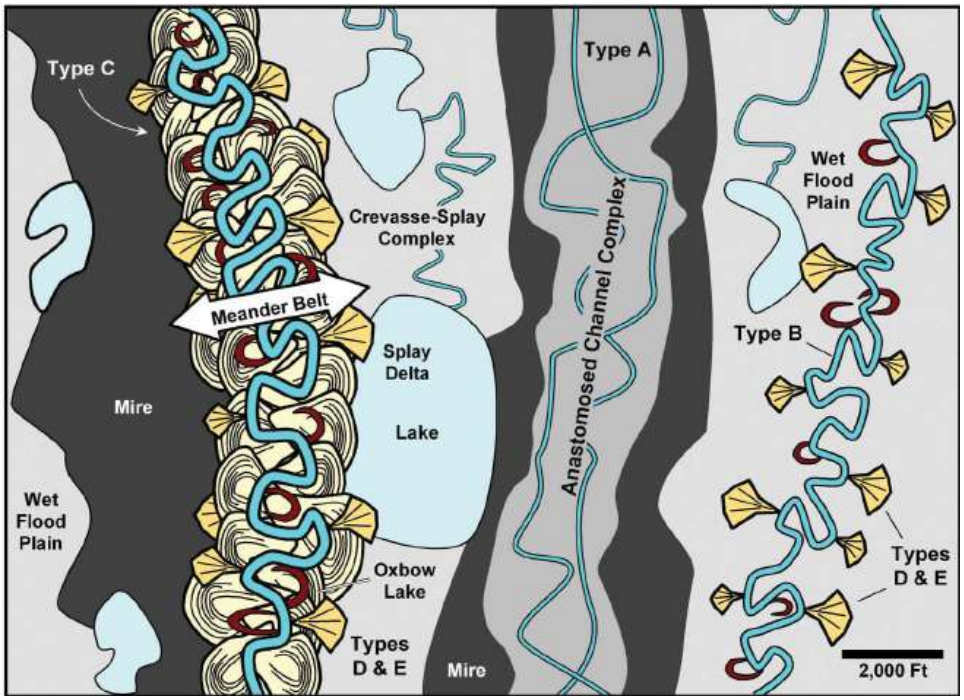

Figure 3.14 Fluvial stratigraphy seen in the Lower Williams Fork Formation (Cole & Cumella, 2005).

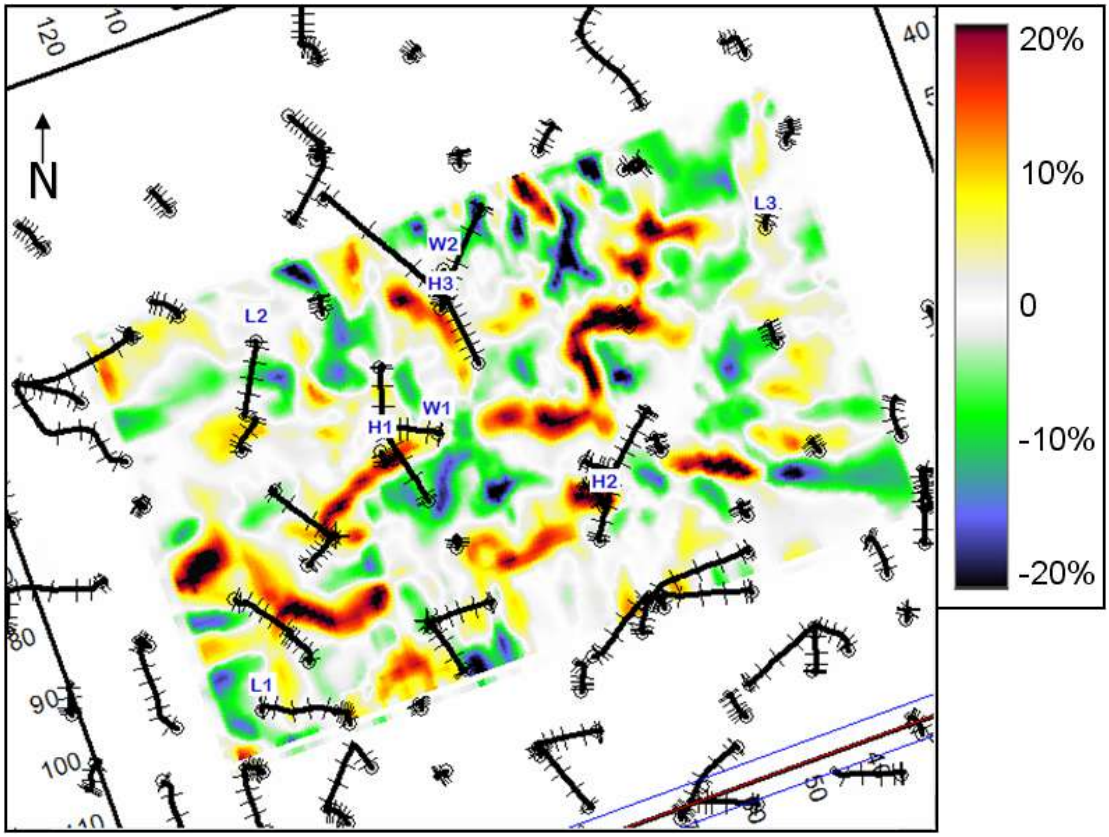

Figure 3.15 Time slice through the similarity difference volume at 2.056 seconds.

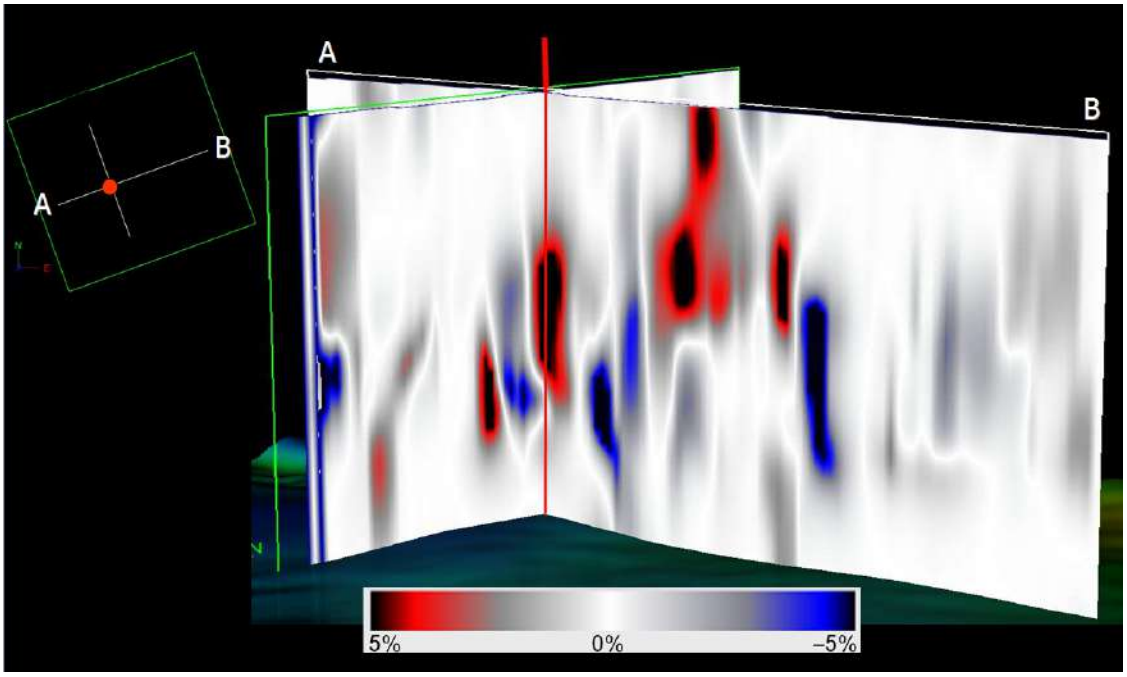

Figure 3.16 Intersecting inline and crossline from the similarity difference volume at well H1 (displayed in red). The top of the vertical seismic sections are at the UMV shale. The

surface cutting through the seismic at the bottom of the image is the Cameo horizon. The wellbore intersects an area of high positive similarity difference in the middle reservoir.

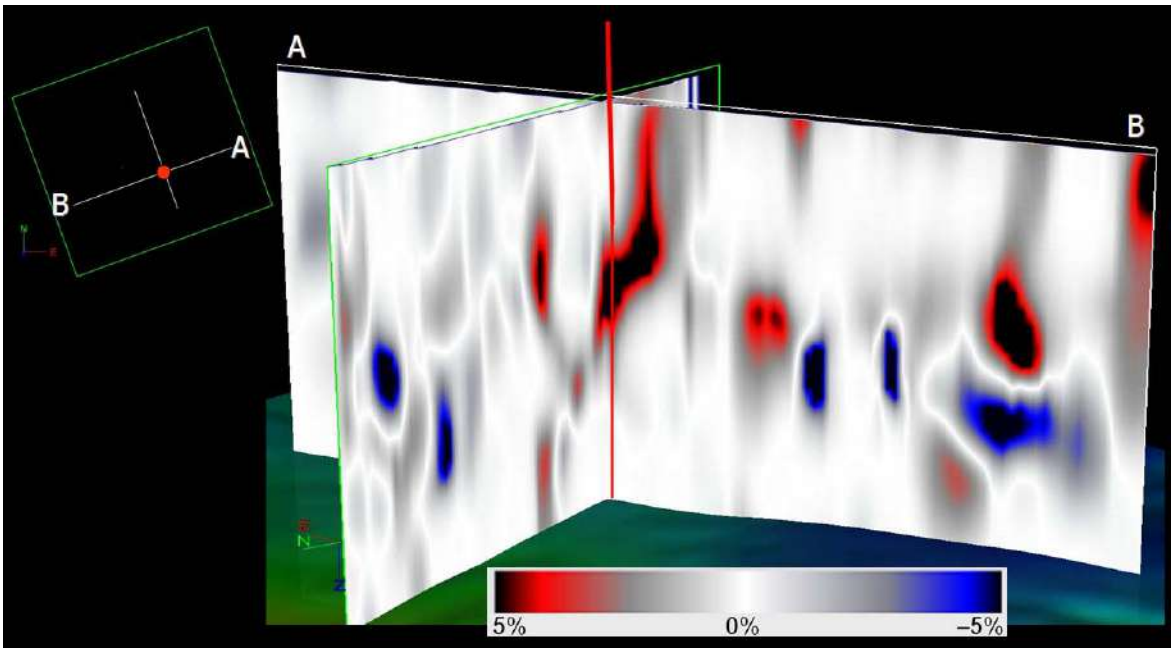

Figure 3.17 Intersecting inline and crossline from the similarity difference volume at well H3 (displayed in red). The top of the vertical seismic sections are at the UMV shale. The surface cutting through the seismic at the bottom of the image is the Cameo horizon. The wellbore intersects an area of high positive similarity difference in the middle reservoir.

3.4 Conclusions

The S-wave splitting analysis presented in this thesis is a viable new method of estimating changes in fracture density the tight gas sand environment at Rulison Field. The anisotropy volume resolved spatial and lateral changes in the fracture density. These variations are similar to the variations in fracture density that are measured in log data. In the high fold area of the survey, the magnitude and variation in anisotropy detected by the volume near well W2 was remarkably similar to the anisotropy log from this well. This volume should be used in field development to estimate the locations of heavily fractured areas and to guide the drilling program.

The similarity difference volume shows the edges between fractured fluvial sandstones and unfractured rock. Well data confirms that many of the anomalies seen by the volume are edges of fluvial sandstones. There is a strong correlation between high positive similarity difference values and high and low EUR wells. All of the high EUR wells are drilled through positive anomalies. These results suggest that the similarity difference volume is detecting the edges of large fractured sandstones. This volume is useful for field development to help select infill well locations.

CHAPTER 4 CONCLUSIONS

From this study, the following conclusions were reached:

- Reservoir level strike-slip faulting can be detected with S-wave seismic.
- The highest EUR wells in the survey are located within a few hundred feet of the faults, and the lower EUR wells are located further away from the faults
- Fracture density generally increases near these faults and creates conduits for natural gas migration.
- Seismic S-wave azimuthal anisotropy accurately detects fracture density in the tight gas sand environment at Rulison Field.
- The similarity difference volume can image the edges of fractured fluvial sandstones.
- The similarity difference volume demonstrates that the geology of the fluvial sandstone reservoir at Rulison Field is very complex and 10-acre well spacing will not fully drain the reservoir.

4.1 Recommendations

Recommendations for future research:

- Refine the procedure used to create the impedance anisotropy and similarity difference volumes.
- Test the S-wave splitting method presented in the thesis with converted-wave seismic.

REFERENCES CITED

Alford, R. M., 1986. Shear Data in the Presence of Azimuthal Anisotropy. Presented at the 56th Annual SEG Meeting. Houston.

Cumella, S. P., and Ostby, D. B., 2003. Geology of the Basin-centered Gas Accumulation, Piceance Basin, Colorado. Piceance Basin 2003 Guidebook: Rocky Mountain Association of Geologists, p171-193.

Davis, G., and Reynolds, S., 1996. Structural Geology of Rocks and Regions: John Wiley & Sons, Inc., p. 369-371.

Davis, T., 2005. Multicomponent Seismic at Rulison Field Overview. Presented at the Reservoir Characterization Project Fall Sponsors Meeting Presentation. Golden, CO.

Fomel, S., Backus, M., Fouad, K., Hardage, B., and Winters, G., 2005. A multistep approach to multicomponent seismic image registration with application to a West Texas carbonate reservoir. Presented at the 2005 Annual SEG Meeting. Houston.

Hargrow, P., 2006. XRMI Processing & Interpretation Williams Production RMT CO RWF 441-20 Garfield, CO: Halliburton, Denver, CO.

Matesic, M., 2006. Interpretation of Structures and Gas Seeps for Well RWF 542-20., in Riley, R.B., ed., The Reservoir Characterization Project Spring 2006 Report.

Jackson, J., 2007, Fracture Modeling and Fault Zone Characteristics Applied to Reservoir Characterization of the Rulison Gas Field, Garfield County, Colorado [Masters Thesis]: Colorado School of Mines, Golden, Colorado.

Jansen, K., 2005, Seismic Investigation of Wrench Faulting and Fracturing at Rulison Field, Colorado [Masters Thesis]: Colorado School of Mines, Golden, Colorado.

Johnson, R.C., and Flores, R.M., 2003, History of the Piceance Basin From Latest Cretaceous Through Earliest Eocene and the Characterization of the Lower Tertiary Sandstone Reservoirs, Piceance Basin 2003 Guidebook: Rocky Mountain Association of Geologists, Denver, Colorado, p. 21-61.

Johnson, R. C., and Nuccio, V.F., 1986, Structural and Thermal History of the Piceance Creek Basin, Western Colorado, in Relation to Hydrocarbon Occurrence in the Mesa Verde Group: AAPG Studies in Geology 73, p. 165-205.

Kuuskraa, V. A., Decker, D., and Lynn, H. B., 1997. Optimizing Technologies for Detecting Natural Fractures in the Tight Sands of the Rulison Field, Piceance Basin, Conference Proceedings of the Natural Gas Conference 1997, paper NG 6-3.

Martin, M.A., and Davis, T.L, 1987, Shear-wave Birefringence: A New Tool for Evaluating Fractured Reservoirs: The Leading Edge, V6, p22-28.

Lancaster, S. and Whitcombe, D., 2000. "Fast-track 'Coloured' Inversion." SEG 2000 Expanded Abstract.

Lorenz, J. C. and Finley, J. S., 1991. Regional Fractures II: Fracturing of Mesaverde Reservoirs in the Piceance Basin, Colorado: The American Association of Petroleum Geologists Bulletin. V. 75, No 11., p. 1738-1757.

Lorenz, J.C., 2004. Fracture Systems in the Piceance Basin: Overview and Comparison with Fractures in the San Juan and Green River Basins. Piceance Basin 2003 Guidebook: Rocky Mountain Association of Geologists, p 75-94.

Riley, R.B., 2007. "Combined Micro-Macro Seismic Monitoring of a Hydraulic Fracture Stimulation, Rulison Field in Wikel, K., ed., The Reservoir Characterization Project Spring 2007 report.

Rumon, M. D., 2006. Shear-wave Time-lapse Monitoring of a Tight Gas Sandstone Reservoir, Rulison Field, Colorado, M.SC. Thesis, Colorado School of Mines.

Sheriff, R. E. and Geldart, L.P., 1995. Exploration Seismology, Cambridge University Press.

Thomsen, L., 1988. Reflection Seismology over Azimuthally Anisotropic Media: Geophysics, v. 53, no. 3, p. 304-313.

Thomsen, L., 2002. Understanding Seismic Anisotropy in Exploration and Exploitation, Society of Exploration Geophysicists.

Toal, B. R., 2005, Piceance Basin. Oil and Gas Investor: Hart Energy Publishing, Houston, Texas.

Topper, R., Spray, K. L., Bellis, W. H., Hamilton, J. L., and Barkman, P. E., 2003, Ground Water Atlas of Colorado: Colorado Geological Survey Special Publication 53. Denver, Colorado. Chapter 6.2.
http://geosurvey.state.co.us/wateratlas/chapter6_2page1.asp

Vasconcelos, I., and Gretcha, V., 2007, Case History: Seismic Characterization of Multiple Fracture Sets at Rulison Field, Colora7do: Geophysics, Vol. 72, No. 2, pB19-B30.